Geophys. J. Int. (2003) **152,** 649–668

Numerical simulation of wave propagation in media with discrete distributions of fractures: effects of fracture sizes and spatial distributions

S. Vlastos,[1,2] E. Liu,[1] I. G. Main[2] and X.-Y. Li[1]

[1] *British Geological Survey, Murchison House, West Mains Road, Edinburgh* EH9 3LA, *UK. E-mail: svl@bgs.ac.uk*
[2] *Department of Geology and Geophysics, University of Edinburgh, Grant Institute, West Mains Road, Edinburgh* EH9 3JW, *UK*

Accepted 2002 September 11. Received 2002 September 6; in original form 2002 May 25

SUMMARY

We model seismic wave propagation in media with discrete distributions of fractures using the pseudospectral method. The implementation of fractures with a vanishing width in the 2-D finite-difference grids is done using an effective medium theory (that is, the Coates and Schoenberg method). Fractures are treated as highly compliant interfaces inside a solid rock mass. For the physical representation of the fractures the concept of linear slip deformation or the displacement discontinuity method is used. According to this model, the effective compliance of a rock mass with one or several fracture sets can be found as the sum of the compliances of the host (background) rock and those of all the fractures. To first order, the background rock and fracture parameters can be related to the effective anisotropic coefficients, which govern the influence of anisotropy on various seismic signatures. We test the validity of the method and examine the accuracy of the synthetic seismograms by a comparison with theoretical ray traveltimes. We present three numerical examples to show the effects of different fracture distributions. The first example shows that different spatial distributions of the same fractures produce different wavefield characteristics. The second example examines the effects of variation of fracture scale length (size) compared with the wavelength. The final example examines the case of fractures with a power-law (fractal) distribution of sizes and shows how that affects the wavefield propagation in fractured rock. We conclude that characterization of fractured rock based on the concept of seismic anisotropy using effective medium theories must be used with caution. Scale length and the spatial distributions of fractures, which are not properly treated in such theories, have a strong influence on the characteristics of wave propagation.

Key words: cracked media, effective medium theory, fractures, finite-difference methods, wave propagation.

1 INTRODUCTION

Numerical modelling techniques are now becoming very common for understanding the complicated nature of seismic wave propagation in fractured rocks. The scientific community has shown an increasing interest in this subject, and currently there are a variety of approaches for forward modelling. Analytic expressions for the description of elastic wave propagation in the presence of fractures are only available for rather simple cases, that is, single cracks with simple geometries (Mal 1970), and in most cases are only valid in the far field (Liu *et al.* 1997). In complex situations, solutions based on Born or Rytov approximations may be used (Wu & Aki 1985). These approximations become accurate in the limit of low-frequency wave propagation and low contrast between scatters and the host rock. However, they have limitations when dealing with large-scale inclusions or fractures such as those encountered in hydrocarbon reservoirs. On the whole, several non-numerical approaches exist for the computation of elastic wavefields that take into account multiple scattering, but few are valid for large sizes and short wavelengths. When the size of inclusions is substantially less than the wavelength, various equivalent medium theories are available (see the review by Liu *et al.* 2000). However, the presence of spatial correlations of different systems cannot be accounted for with any effective medium theory. Therefore, the use of numerical methods seems to be the only way that is capable of providing accurate solutions without a restriction of the size-to-wavelength ratio.

The numerical techniques employed so far to study seismic wave scattering problems include the Maslov theory (Chapman & Drummond 1982), the finite-difference method (FD) (van Baren

et al. 2001; Saenger & Shapiro 2002), the pseudospectral method (PS) (Fornberg 1988), the finite-element method (FE) (Lysmer & Drake 1972), the boundary element method (Benites *et al.* 1992; Pointer *et al.* 1998; Liu & Zhang 2001) and the spectral finite-difference method (Mikhailenko 2000). In this study we use the pseudospectral method to simulate wave propagation in media with discrete distributions of fractures. In contrast with the widely used FD method, the PS method substitutes the spatial difference scheme with a Fourier and inverse Fourier transform pair. A minimum of two nodes per wavelength (theoretically) is needed to obtain an accurate derivative, compared with FD which normally requires 10–20 nodes per wavelength (Alford *et al.* 1974). This is one of the major advantages of the PS method. However, there is a drawback in the use of the PS method. It intrinsically treats all physical quantities as spatially periodic and, as a result, all energy transmitted and reflected through the boundary will travel back into the grid. These artefacts often mask important features of real modelled signals. This deficiency can be mitigated by modifying the wavelet near the grid boundary in such a way that the wave amplitude is attenuated.

Fractures with a vanishing width in the 2-D finite-difference grids are implemented using an effective medium theory (following Coates & Schoenberg 1995). In the literature, there have been several such theories that attempt to predict effective properties of a rockmass containing distributed fractures. In this paper,

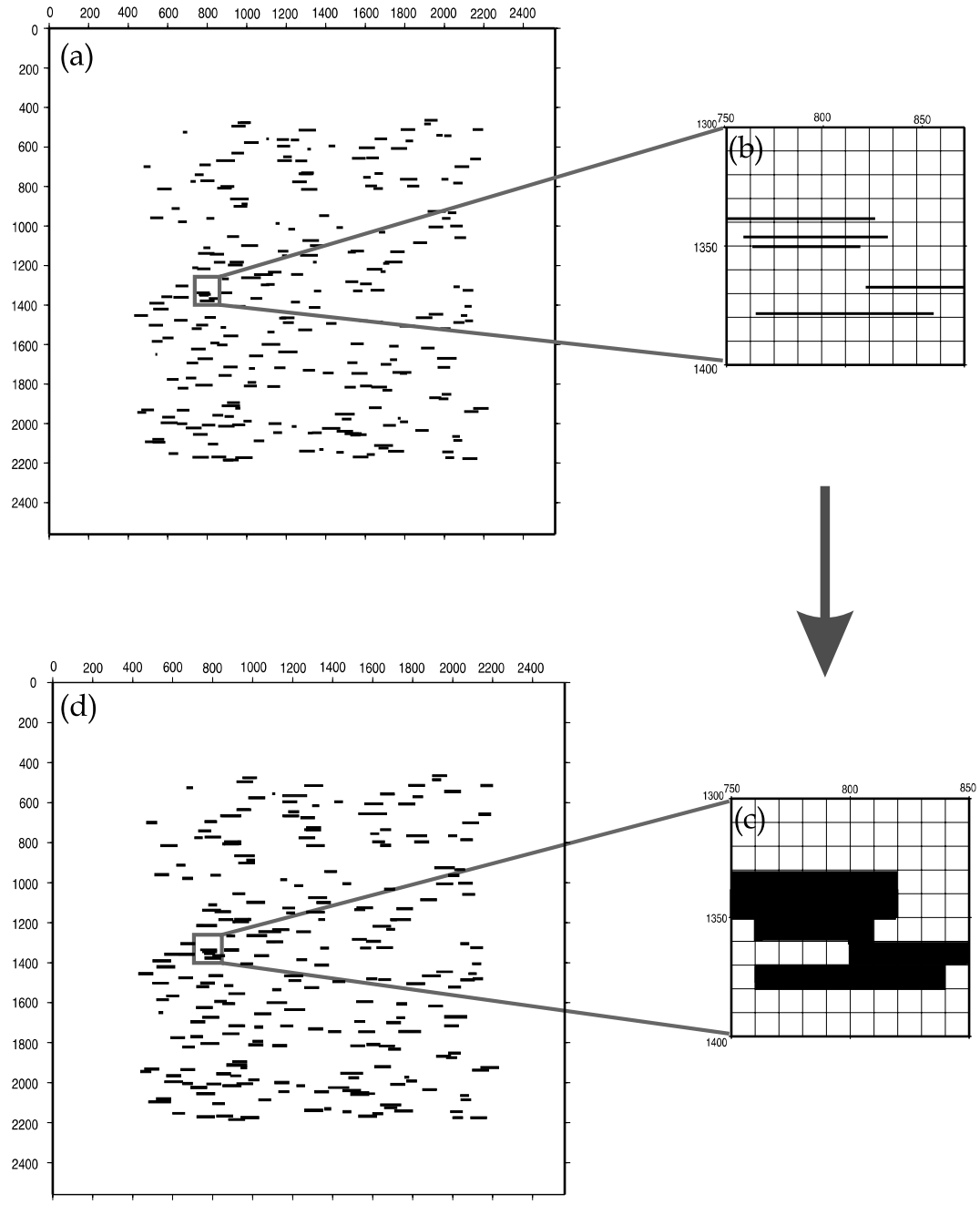

Figure 1. Schematic illustration of fracture discretization in the finite-difference grid. In (a) we show the fractured medium that we want to examine. In (b) we present a very small area of the whole model and (c) shows the same area discretized in the FD grid. Finally, (d) shows again the whole medium where, this time, the fractures are discretized. By comparing (a) and (d) we can see the high accuracy of the discretization.

fractures are treated as highly compliant interfaces inside a solid rock mass. We represent the fractures using the displacement discontinuity method (DDM) by Schoenberg (1980). We examine the validity of the method, and test the accuracy of the synthetics produced from the modelling. We choose a simple case to model and compare the synthetic seismograms with the theoretical ray traveltimes. After testing the method, we present some numerical examples. First, we examine the effect of the spatial distribution of fractures on the wavefield propagation. Secondly, we examine different sizes of fractures, having the same spatial distribution, and we attempt to associate the different features of the waveforms with the attributes of the fractures, and in particular their sizes. Finally, we model the scattering of the wavefield by fractures with a scale length distribution. The fractures in our model follow a power-law or fractal distribution up to a maximum length smaller than the model space, that is, below the percolation threshold. Power-law size distributions are the most common form encountered in natural data sets where a broad bandwidth of data is available (Bonnet *et al.* 2001).

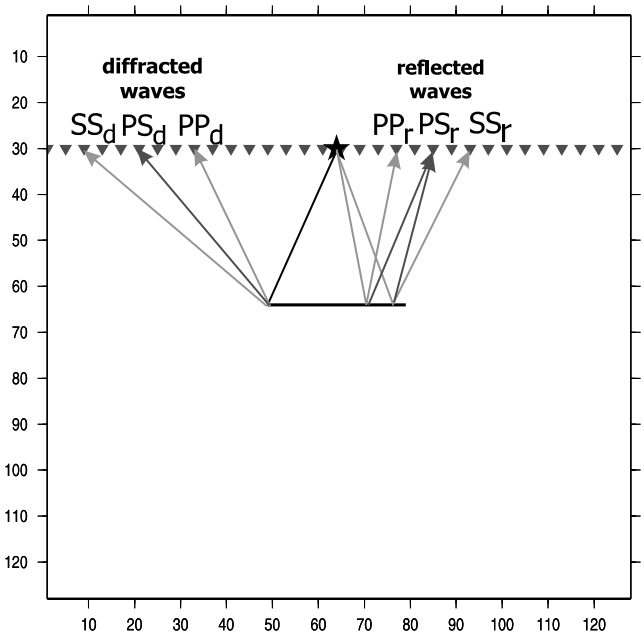

Figure 2. Schematic representation of the model used for the testing of the accuracy of the modelling method, and representation of the ray paths of the different kind of waves generated by the source that interact with the fracture.

2 IMPLEMENTATION OF FRACTURES (THE COATES AND SCHOENBERG METHOD)

To obtain the effective parameters of fractured media, fractures are treated as infinitely thin highly compliant interfaces inside a solid rockmass. Following the concept of the linear slip deformation or displacement discontinuity model of Schoenberg (1980), a fracture can be represented as a boundary across which the displacements are discontinuous, whereas the stresses remain continuous. To first order the displacement discontinuity and the tractions are linearly related, i.e.

$$[u] = \boldsymbol{Z}\tau, \tag{1}$$

where $[u]$ is the average displacement discontinuity, τ is the traction acting across the fracture and $\boldsymbol{Z}$ is called the fracture compliance

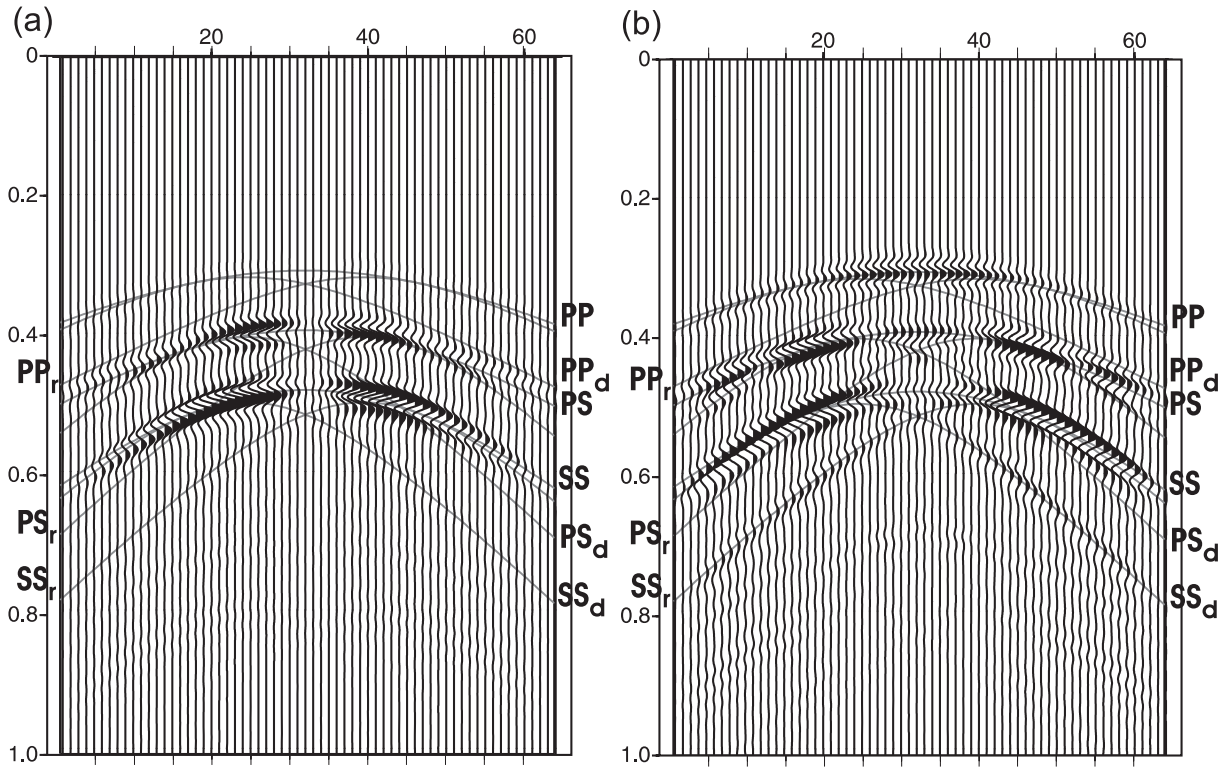

Figure 3. Comparison between the theoretical ray traveltimes and the synthetic seismograms generated by the modelling method. We present (a) the horizontal (x) and (b) the vertical (z) components of the seismograms. As we can see from the figure they are in very good agreement with the theoretical traveltimes, thus verifying the accuracy of the method.

tensor, which is an elastic parameter of the medium. This linear relationship is consistent with the usual seismic approximation of infinitesimal strain. In addition, there has been some experimental verification of the DDM model by Pyrak-Nolte *et al.* (1990) and Hsu & Schoenberg (1993). Essentially, eq. (1) is a boundary condition of the fracture surfaces. In a finite-difference algorithm, the relationship can be implemented by requiring a displacement jump across gridpoints on either side of the interface, proportional to the local (continuous) stress traction. The implementation of the displacement jump is relatively simple, even with $\boldsymbol{Z}$ being a function of position on the fault plane, providing the interface lies along a given plane of the finite-difference grid. In nature, fractures have finite length. To implement a finite fracture we take $\boldsymbol{Z} = 0$ at locations on the plane exterior to the fracture. The question that remains is how to implement the constraint that $\boldsymbol{Z} \rightarrow 0$ on the tips of the fracture. We taper off the value of $\boldsymbol{Z}$ following the formulation of the crack-opening displacement introduced by Kachanov (1984). The value of $\boldsymbol{Z}$ has its maximum value in the centre of the fracture and reduces to 0 at both fracture tips following a hyperbolic pattern. The rate at which the value of compliance reduces depends strongly on the length of the fracture.

In the finite-difference method, the medium is discretized into small rectangular grids and we find the elastic parameters of the equivalent medium for each grid cell. For each grid intersected by a fracture (or portion of fracture), the elastic medium within the cell surrounding the fracture, together with the embedded segment of the fracture, are replaced by an equivalent anisotropic medium. Muir *et al.* (1992) showed how the elastic parameters could be found for a cell enclosing an interface between two elastic media. The discretization of the fracture in the finite-difference grids is shown schematically in Fig. 1. This method was first used by Coates & Schoenberg (1995), and therefore it is referred to as the Coates and

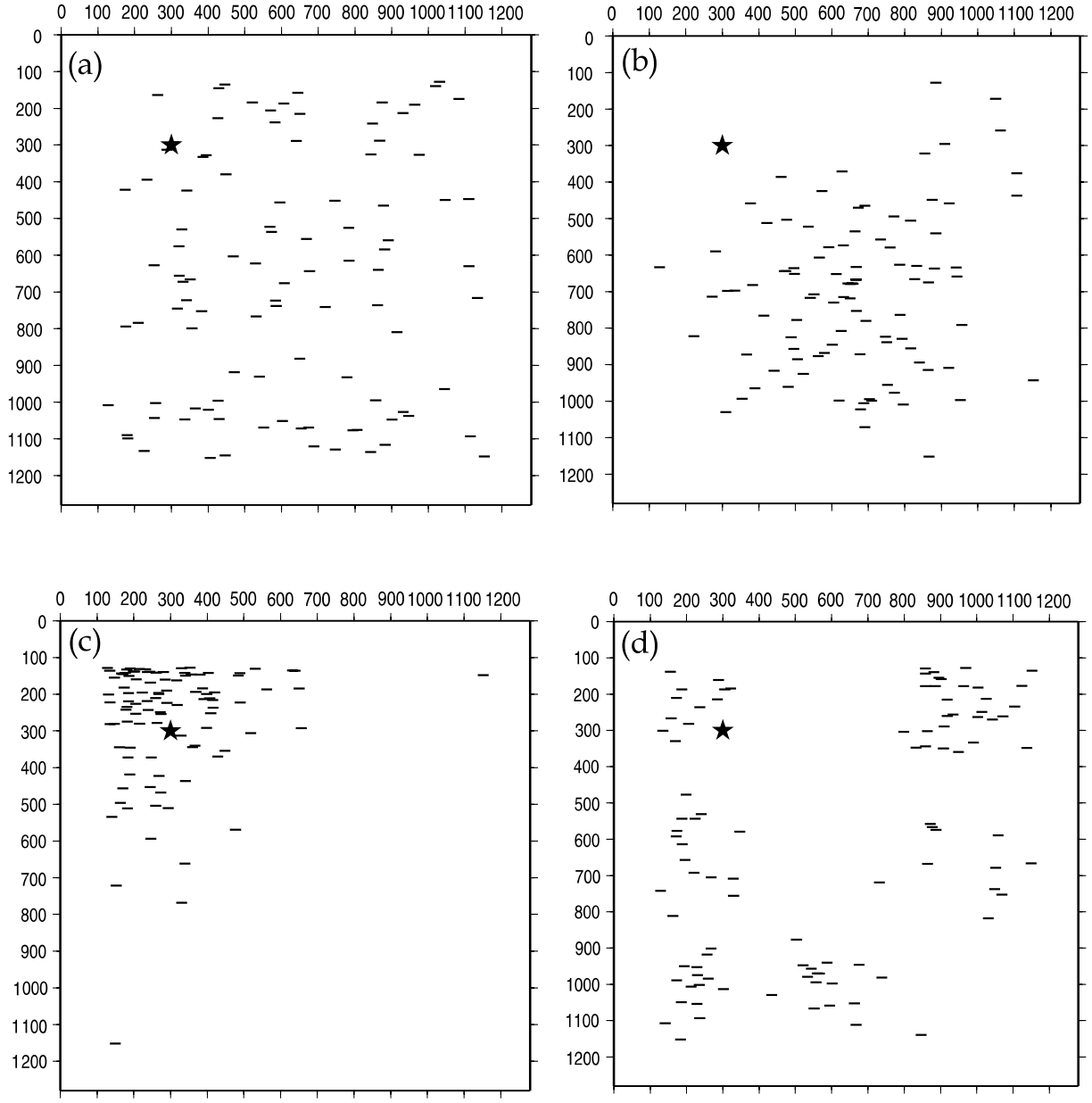

Figure 4. Example 1: model used to compute snapshots from spatially distributed fractures. The four different models, (a)–(d), illustrate different statistical distributions of fractures. *P* and *S* waves are generated at the source (represented by a star) and travel inside the medium.

Schoenberg method in this paper. In Fig. 1(a) we show the whole fractured medium. Then we take a very small area of the medium in Fig. 1(b), to show how the fractures are represented in the finite-difference grid. Fig. 1(c) shows the discretization of the fractures in the grid, where the shaded areas are the finite-difference grid cells intersected by one or more fractures, whilst the plain areas are the cells that include only the background rock. Finally, in Fig. 1(d) we show the whole medium again, but this time each cell is either shaded or plain, depending on whether fractures are present. By comparing Fig. 1(d) with Fig. 1(a), where we show the medium with the actual fractures, we can see that the discretization of the fractures is very accurate. In the numerical examples presented in this paper we use in some cases a grid size of 128×128 and in other cases 256×256. The grid cell size is very important for the discretization of the fractures. To achieve high accuracy, we choose grid sizes smaller than or equal to the size of the smallest fractures. Thus any size of fracture can be represented accurately by the elastic parameters of the effective medium in each finite-difference grid cell. The variables required for the effective medium calculation in each cell are the length of the fracture, its orientation and the local value of the fracture compliance tensor. In the numerical models that will be presented later, fractures are represented as finite lines for which we know the starting and the ending points. Using simple algebra we can define the equation of any line that passes between two points. Knowing the equation that describes each fracture, we can locate the intersections of the fractures with the horizontal and vertical boundaries of each cell (if any) and calculate the length and orientation of the fracture segment lying in each cell. The effective medium for each cell may then be calculated using these values and the method for estimating the fracture compliance tensor outlined in Appendix A. The tapering of the value of the fracture compliance $\boldsymbol{Z}$ is explained in detail in Appendix B.

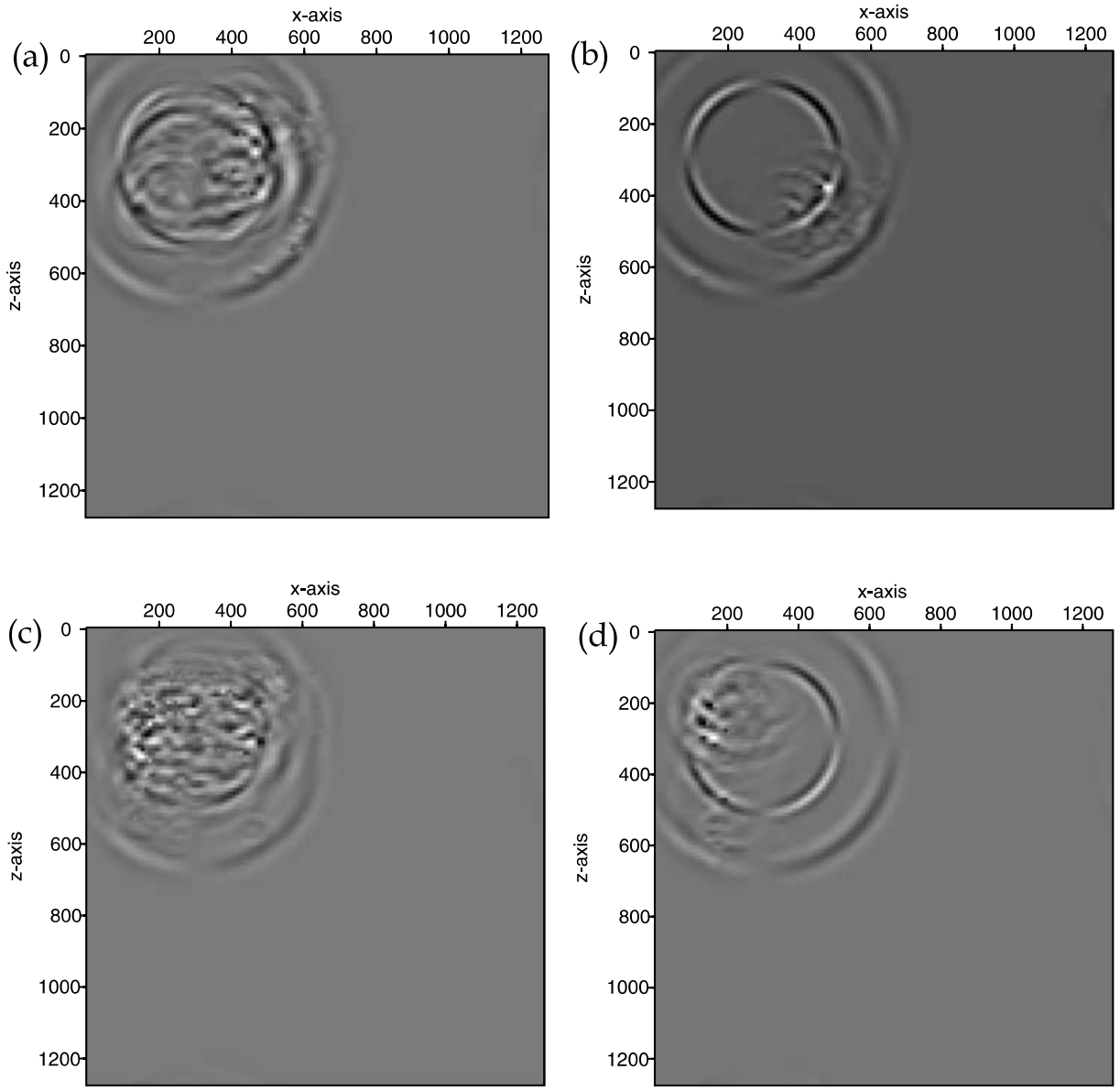

Figure 5. Snapshots taken at $t = 100$ ms. (a)–(d) correspond to fracture distributions (a)–(d) in Fig. 4. The numbers on the top and on the left-hand side of the snapshots are the model dimensions. We present the x-component of motion.

3 VALIDATION

The first step is to compare results generated by our modelling method with those obtained by another method. This has been done by Coates & Schoenberg (1995), Nihei & Myer (2000) and Nihei *et al.* (2000), who compared the synthetic seismograms from the Coates and Schoenberg method described with the exact solutions using boundary element methods. We assess the accuracy by comparing the synthetic seismograms generated by the modelling with the ray theoretical traveltimes.

The model geometry used for accuracy testing is shown in Fig. 2. The source, receivers and fracture are situated in an ideal elastic ($V_P = 3300$ m s^{-1}, $V_S = 1800$ m s^{-1}, $\rho = 2200$ kg m^{-3}) full space. The receiver array at which vertical and horizontal particle displacements are recorded is horizontal and 340 m above the fracture. The fracture is 300 m long. The source is located at the centre of the receiver array. The source type is a vertical force. The source signal is a Ricker wavelet (Ricker 1977) with a peak frequency of 25 Hz and a pulse initial time of 0.1 s. Fig. 2 also shows the different kinds of waves created by the interaction of the waves generated by the source and the fracture. The source generates both *P* and *S* waves. When they reach the fracture boundary those waves are reflected and we have PP_r, PS_r, SP_r and SS_r waves. PP_r-waves will be the first to arrive at the receivers. Those are waves that travel both before and after the reflection as *P* waves. The next arrivals will be the PS_r and SP_r waves. The PS_r waves travel as *P* waves from the source to the fracture, and as *S* waves from the fracture to the receivers. In the case of the SP_r waves, the case is the complete opposite. The arrival of those two different types of waves happens at the same time, because the source–fracture and fracture–receiver distances are equal. As a result, the distance that they travel as *P* and as *S* waves is exactly the same in both cases, so we present both of them as PS_r waves in Fig. 2. Finally, the SS_r waves arrive at the receivers, which travel both legs as *S* waves. In addition to the reflected waves, there are waves diffracted from the crack tips. We have *P*- and *S*-wave diffractions, and also conversion from *P* to *S* waves and vice versa, which are

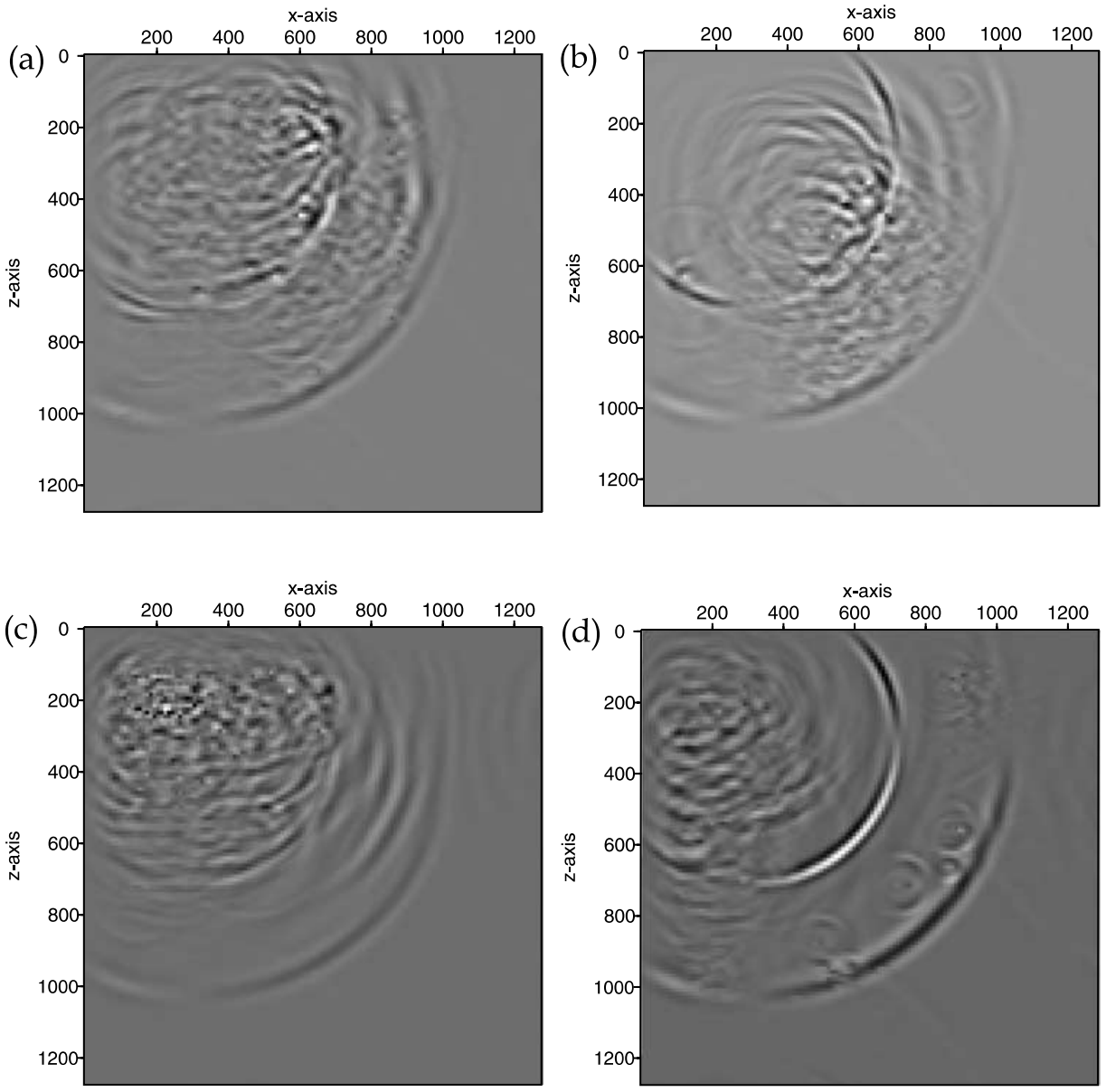

Figure 6. Snapshots taken at $t = 200$ ms.

diffracted from the tips of the fracture. These waves are presented in Fig. 2 as PP_d, PS_d, SP_d and SS_d waves.

We calculate the theoretical ray traveltimes and overlap them on the synthetic seismograms. Figs 3(a) and (b) show the horizontal (x) and the vertical (z) components, respectively, of the synthetic seismograms together with the theoretical ray traveltimes. As we can see from both figures, we have very good agreement between the theoretical ray traveltimes and the synthetic seismograms. All types of waves are accurately represented in the synthetic seismograms. Owing to the type of source that we implement, we have strong arrivals at short offsets on the horizontal component and strong arrivals at long offsets on the vertical component. In addition to that, the diffracted waves from the tips of the fracture and the PP_r and PP_d waves are not visible in the horizontal component, but they are very clearly demonstrated in the vertical component and follow the theoretical traveltimes. This is expected because the source causes vertical displacements on the medium, so very close to the source and very far away from it, the horizontal displacement is negligible.

Another aspect of the comparison between the theoretical and the modelled data is that they give us further insight into the waveform patterns. For instance, we can see in both Figs 3(a) and (b) that in the areas of superposition between the reflected waves from the fractures and the diffracted waves from the tips we have maximum amplitude in the wavefield, as a result of constructive interference. This gives us valuable information concerning the medium we are examining.

4 NUMERICAL EXAMPLES

The PS method has been used to model the seismic wavefield reflected and diffracted by fractures. We examine the influence of different fracture parameters on the displacements. In particular, we are interested in understanding the effects of spatial distributions, the scale length distribution of fractures and looking for characteristics in the wavefields owing to different distributions.

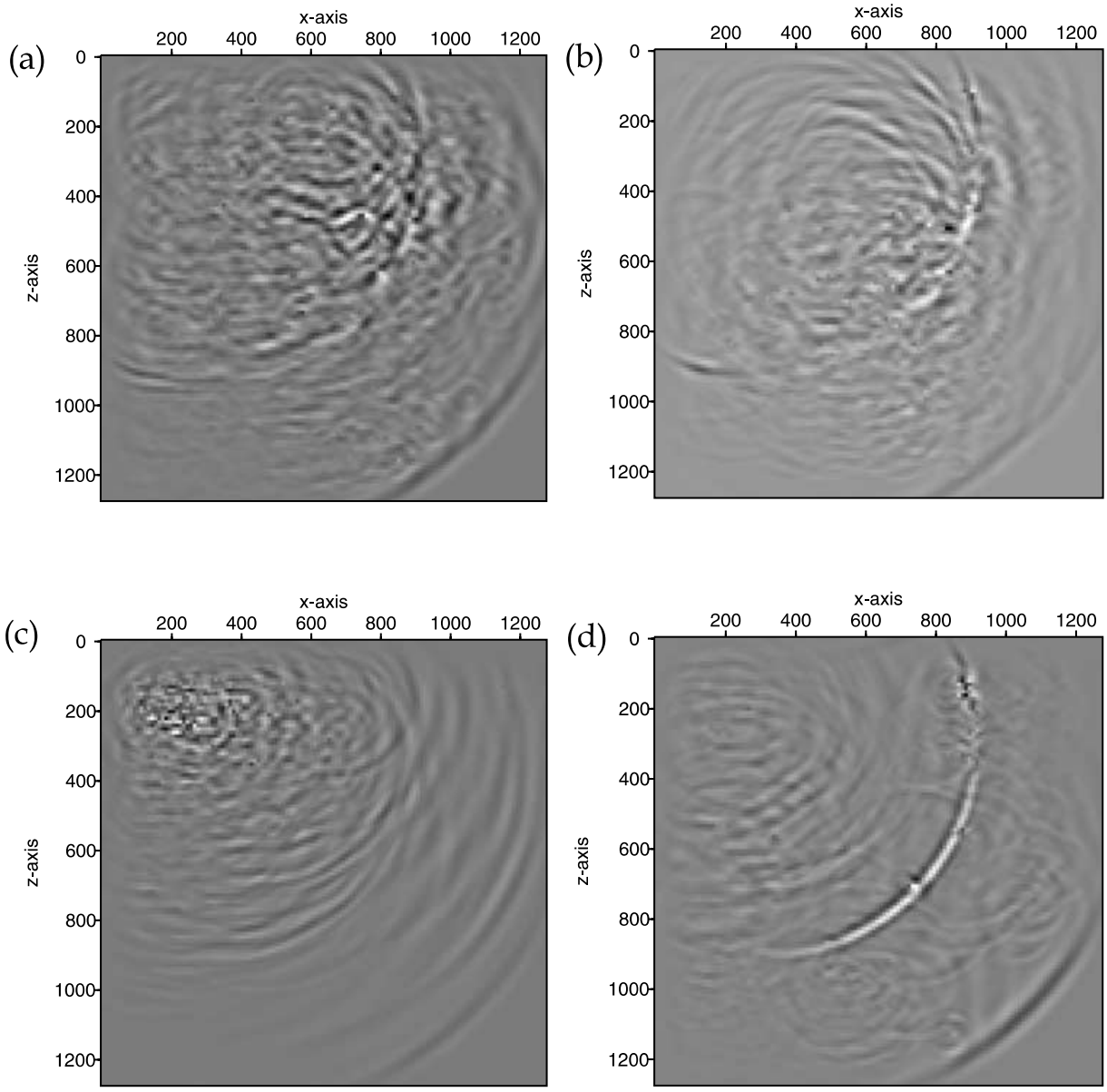

Figure 7. Snapshots taken at $t = 300$ ms.

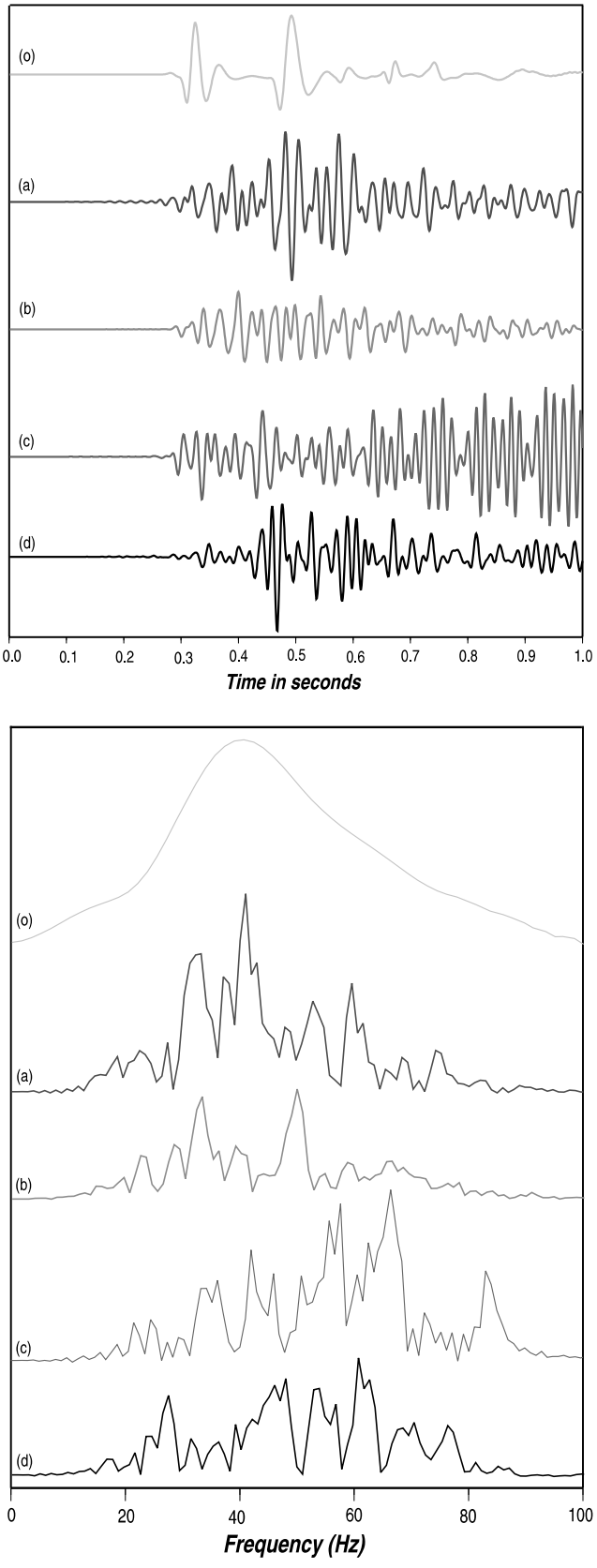

Figure 8. Comparison of synthetic seismograms and corresponding spectra from various distributions of fractures: (o) no fractures, (a)–(d) correspond to the fracture distributions of Fig. 4 (trace number 100).

4.1 Fracture spatial distribution

The first example is given in Fig. 4, in which we attempt to model four different simulations of random fracture distributions. In each model, there are 100 fractures randomly distributed in a 1280 × 1280 m^2 area. To create the various random distributions of fractures we used an algorithm that generates four arbitrary distributions, featuring different qualitative characteristics. We use parent distributions for the fracture centre spacings that are (a) random uniform, (b) Gaussian, (c) exponential and (d) Gamma distribution. In the cases where we have overlapping of fracture positions, we remove the overlapping fractures and generate new fractures until the desired number of fractures is reached. As a result of this process, the final crack distribution is not necessarily random. Nevertheless, the purpose of this paper is to illustrate how different distributions affect multiple scattering. The generation of the different fracture distributions is presented in detail in Appendix C. In this simulation, each fracture has the same length, $2\alpha_c = 30$ m, where α_c is the radius or the half-length of the fracture. The surrounding solid (matrix) has P- and S-wave velocities $V_P = 3500$ m s^{-1}, $V_S = 2000$ m s^{-1} and density $\rho = 2200$ kg m^{-3}. The source is located at the left-hand corner of the model. The source type is a vertical force. A Ricker wavelet with a dominant frequency of 40 Hz is used, so that $k_p\alpha_c = 1.08$ and $k_s\alpha_c = 1.88$ (where $k_p = 2\pi f/V_P$ and $k_s = 2\pi f/V_S$ are the P and S wavenumbers), or equivalently $\lambda_p/2\alpha_c = 2.9$ and $\lambda_s/2\alpha_c = 1.67$ (where $\lambda_p = V_P/f$ and $\lambda_s = V_S/f$ are P and S wavelengths, respectively). For demonstration purposes, in all models in the paper we have used fracture compliance $Z_N = Z_T = 5.6 \times 10^{-10}$ G Pa^{-1} at the elementary scale.

The resulting snapshots taken at $t = 100$, 200 and 300 ms are given at Figs 5–7, respectively. As we can see from Fig. 4, fractures are more clustered in models (b) and (c), whereas they are more uniformly distributed or more scattered in models (a) and (d). In the extreme case of model (c), where the fractures are exponentially distributed, they are all concentrated in a small area around the source, forming a big cluster. This results in a lot of energy being trapped inside the cluster, between the various fractures. We observe the effect of the high clustering in the snapshots of the wavefield propagation at consecutive times, concentrating mainly on the mean wavefield. The wave fronts shown on the snapshots represent the statistical average effect of the fractures encountered throughout the wave path, thus resulting in a mean wavefield. The energy attenuation becomes clearer at 300 ms, where we see a lot of energy remaining in the area of the fracture cluster, whereas the mean wavefield almost does not exist. In model (b) where the fractures follow a Gaussian distribution, the fractures also form a big cluster in the centre of the model, but in this model they occupy more space and the distance between the various fractures is greater. In this case, similar to model (c), we have a significant amount of energy trapped in the fracture cluster. However, we can observe from the snapshots that there is more energy coming through the cluster, and that gives a fairly clear image of the mean wavefield of at least the P wave. The opposite case to the two previous ones is described in model (d). In this case the fractures follow a Gamma distribution (a power law with an exponential tail), thus forming a number of small clusters that are significantly distant from each other. It is observed in the snapshots that in this case the mean wavefield, for both P and S waves, is most clearly observed and has the highest amplitude compared with the rest of the cases. We believe that the small size of the clusters formed means that a lot of energy is not kept inside them, letting most of the energy propagate through the whole model. Finally, model (a)

where fractures are randomly uniformly distributed, describes a case where we do not have any clustering. The fractures are distributed throughout the whole medium. Although the snapshots show some trapped energy between the fractures, the mean wavefield propagation is quite clearly observed. To sum up the results, we can see that the wavefield propagates with the least energy attenuation when we have the least fracture clustering as shown in model (d), while attenuation increases with increasing clustering as shown in models (a)–(c), respectively.

In the following, we take the models of Fig. 4 and calculate the synthetic seismograms. The receivers are positioned along the z-direction and shifted by 1050 m in the x-direction. The cases we compare are (o) no fractures, (a) random uniform distribution, (b) Gaussian distribution, (c) exponential distribution and (d) Gamma distribution. Fig. 8 shows comparisons of waveforms of the x-component of motion from trace number 100, that corresponds to the depth of 1000 m, of each of the models and their corresponding Fourier spectra. In the figure we observe a noticeable shift of energy to frequencies higher than the dominant frequency. If we compare the global maxima for all the cases examined, we can see in model (a) that the maximum energy is at approximately 40 Hz, which is the source dominant frequency, in model (b) it is at approximately 49 Hz, in model (c) it goes up to approximately 67 Hz, and in model (d) it is at 60 Hz. In terms of the distance that the wave travels between two consecutive scatterings, in model (a) we have the longest distance and in model (c) the shortest. Combining that with the observation that in model (a) we have no frequency shift of the energy, while in model (c) we have the maximum frequency shift indicates that there is a systematic shift of energy to higher frequencies when the multiple scattering dimension becomes shorter. Another feature of the spectra is the local minima of the amplitude. The first local minimum is observed at 30 Hz where the length of the fractures is approximately a quarter wavelength. There are also local minima at around 38, 58 and 70 Hz. These minima can be a result of the constructive or destructive interference of multiply scattered waves from the fractures. Finally, we notice that the

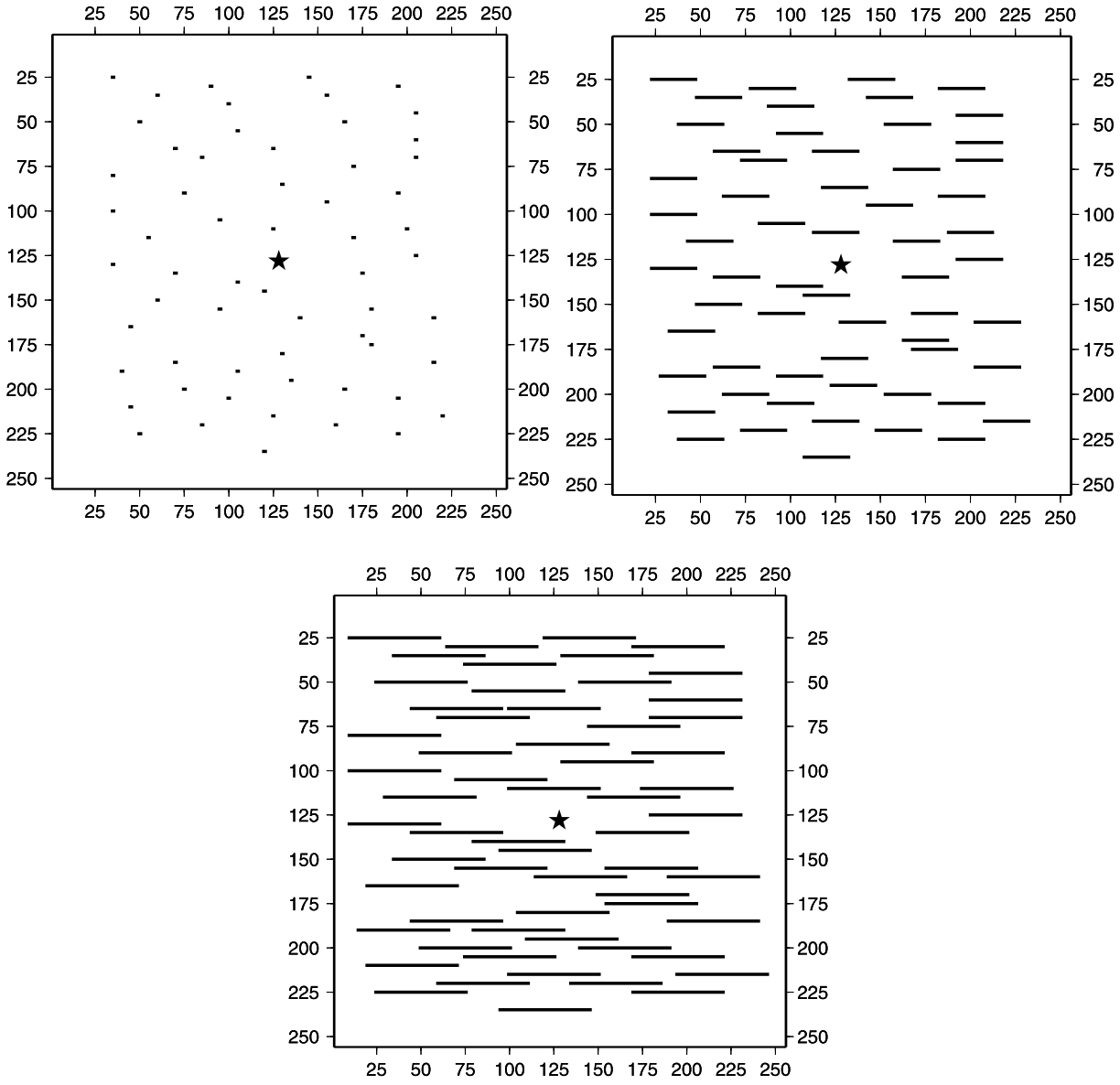

Figure 9. Example 2: model used to compute snapshots from randomly distributed fractures having different sizes compared with the source wavelength: (a) $\alpha = 0.1\lambda$, (b) $\alpha = \lambda$ and (c) $\alpha = 2\lambda$.

amplitude of the wavefield from distribution (b) is much smaller and has a relatively low-frequency content compared with the other distributions. This is possibly because in this case the local fracture density along the wave path towards the receivers is higher compared with the other cases. This example demonstrates clearly that different distributions of fractures have a significant influence on multiple scattering.

4.2 Effects of fracture scale length

The second example is used to examine wave scattering in a fractured medium where fractures have different sizes compared with the source wavelength. To ensure consistency of the results from different models we use the same background medium in all cases, which guarantees that any variation in the features of the wavefield is a result of the variation in the size of the fractures. The matrix parameters are $V_P = 3300$ m s^{-1} and $V_S = 1800$ m s^{-1} for the *P*- and *S*-wave velocities, respectively, and the density is $\rho = 2.2$ g cm^{-3}. The source is a vertical force and is located at the centre for all the models. The source wavelet is a Ricker wavelet with a dominant frequency of 25 Hz and a initial pulse time at 0.1 s. We use a grid size of 256 × 256, with a spatial grid step of 10 m and a time step of 0.001 s. In all the models we have 50 fractures that follow a completely random distribution to avoid clustering patterns. We examine three different cases of fracture sizes, $\alpha_c = 0.1\lambda$, $\alpha_c = \lambda$ and $\alpha_c = 2\lambda$, where α_c is half the fracture length and λ is the wavelength.

Fig. 9 shows the models of the different sizes of fractures we examine, while Fig. 10 shows the respective snapshots taken at 350 ms. We observe in model (a) that when the wavelength is larger than the size of the fractures, we have a clear image of the propagation of *P* and *S* waves through the fractured medium, and each individual fracture acts as a point scatterer that becomes a secondary source. On the other hand, when the size of the fractures is equal to or larger

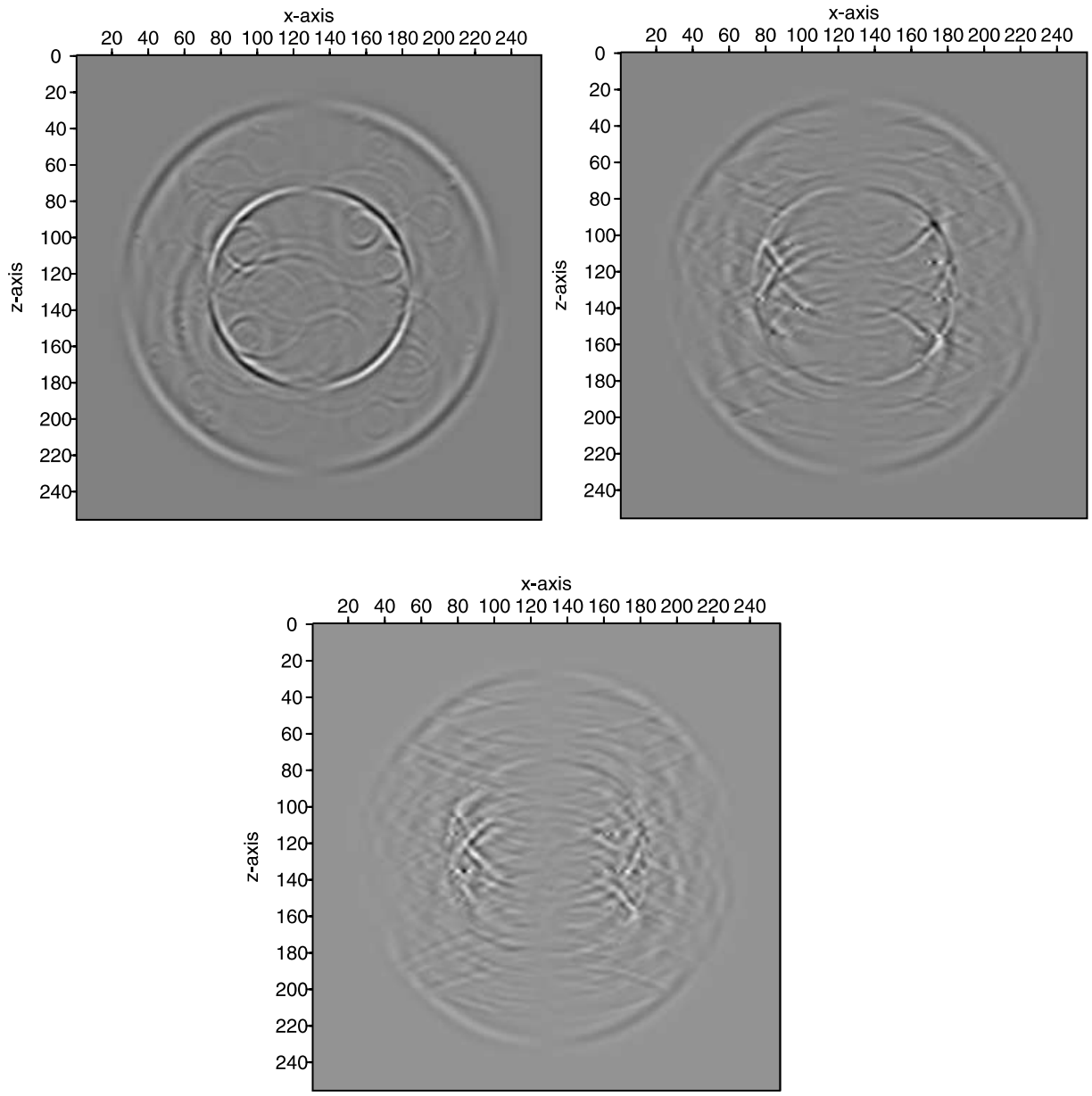

Figure 10. Snapshots taken at $t = 350$ ms. (a)–(c) correspond to fracture models (a)–(c) in Fig. 9. The numbers on the top and on the left-hand side of the snapshots are the model dimensions. We present the *x*-component of motion.

than the wavelength, they act almost as individual boundaries and the amplitudes of the reflected waves depend on the interference between the various reflections. In addition, following the results of the previous section on the effects of the fracture distribution together with the effects of the scale length, strong and coherent energy will be present in areas of high fracture clustering where fractures form large clusters and have a large size, thus acting as a single reflector.

4.3 Power-law (fractal) distribution of fracture sizes

The final example is used to model wave scattering from discrete fractures with a scale length distribution. The model we use is given in Fig. 11(a), where the variation of crack sizes follows a von Kármán correlation function, which gives a power-law distribution (Wu 1982). We can also use other correlation functions, such as Gaussian or exponential functions. The model shown in Fig. 11(a) is generated with a correlation length of 40 m. In this model we have 400 fractures randomly distributed in a 2560 × 2560 m^2 area. The source is a vertical force and is located in the centre of the model, and is represented by a star in Fig. 11(a). The longest fracture is 100 m and the shortest is 10 m. The mean length of the fractures $\langle a \rangle$ is 27.5 m, and the fracture density of the medium $\varepsilon = N_f \langle a \rangle^2 / S$ is 0.046, where N_f is the number of fractures and S is the surface of the medium. The peak frequency is 40 Hz, which gives α ranging from 0.36 to 3.6 for P waves and from 0.63 to 6.3 for S waves, where k is the wavenumber, the P-wave velocity is 3500 m s^{-1} and the S-wave velocity is 2000 m s^{-1}. Figs 11(b)–(d), illustrate the attributes of the size distribution of the fractures. Fig. 11(b) shows the different sizes of fractures in the model of Fig. 11(a). Fig. 11(c)

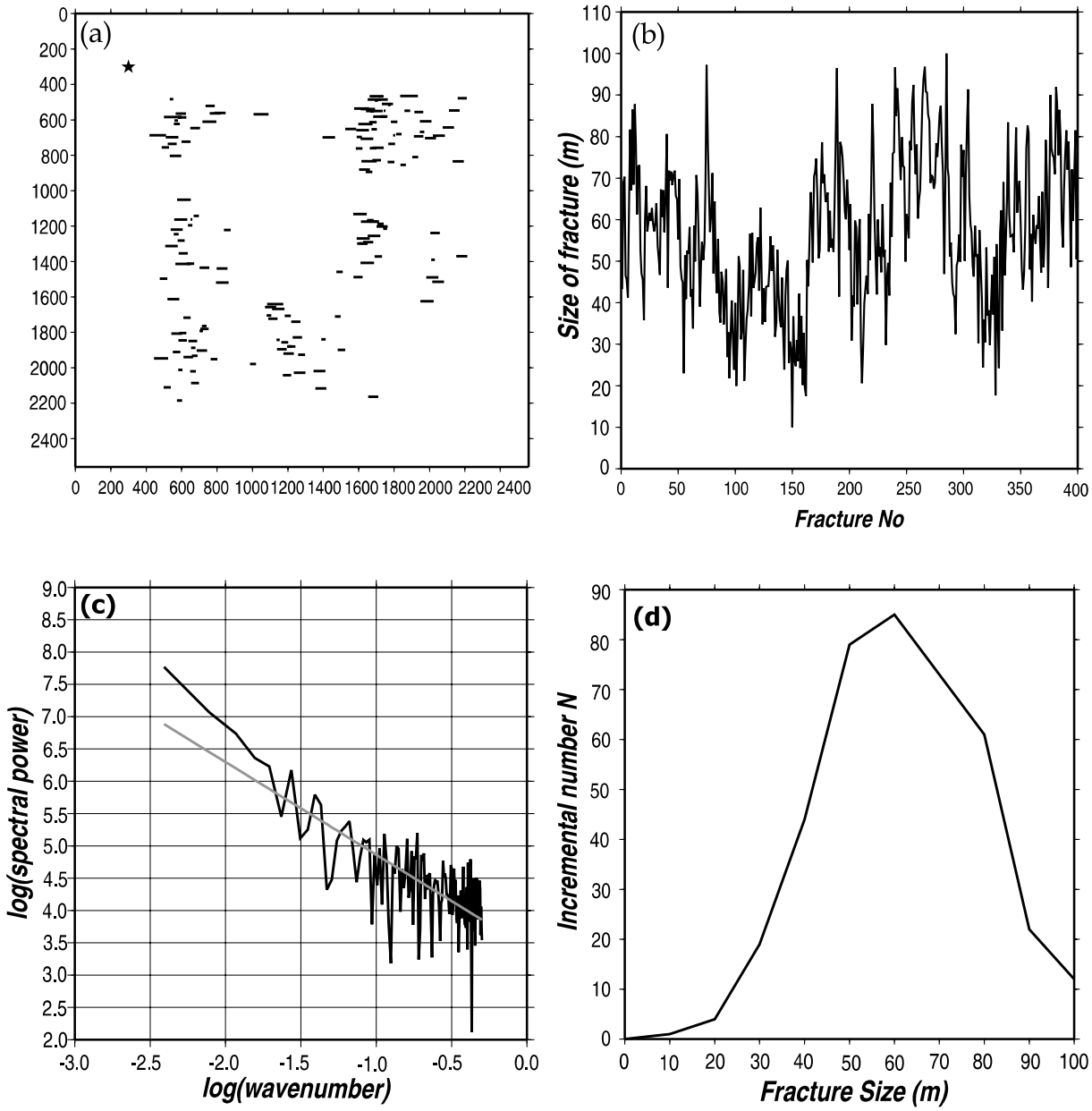

Figure 11. (a) Example 3: model used to compute synthetic seismograms from fracture distribution with power-law distribution of fracture sizes. (b) Illustration of the sizes of fractures in model (a), that follow a power-law distribution. (c) Power spectra of fracture size distributions shown in (a). (d) Cumulative number of the fractures of model (a) plotted against the fracture size.

shows the power spectrum of the fracture size distribution presented in Fig. 11(a) (plotted on a log–log scale). We see that the variation can be fitted with a straight line. Such a model (i.e. with a linear variation of the logarithm of the power spectrum with the logarithm of the spatial wavenumber) is a power-law distribution, often called a fractal (Bonnet *et al.* 2001). Fig. 11(d) shows the variation of the incremental number of the fracture population in the corresponding range of fracture sizes. To examine the behaviour of the wavefield arising from the fractal distribution of fractures in the medium, we take snapshots at consecutive times, $t = 200$, 250, 300 and 350 ms. The snapshots are presented in Fig. 12. As we can see from the snapshots, the behaviour of the wavefield is very complicated. Clearly, the *P* and *S* mean waves are fading away as they propagate through the medium. This can be attributed to the scattering taking place as the wavefield propagates through the high fracture density clusters. This is confirmed by the snapshots, where we can see high energy concentrated at the exact positions of the fracture clusters. This is particularly clear in Fig. 12(d), where we have high amplitudes in the areas of fracture clusters resulting in strong coda waves, and at the same time low amplitudes of the mean *P* and *S* waves.

5 CONCLUSIONS

We have used the pseudospectral method to study the effect of different attributes of fractures on the wavefield characteristics. The fractures have been implemented in finite-difference grids using an effective medium theory. The method can deal with multiple scattering cases without having any limitations on the number of fractures included in the medium. The representation of the wavefield is highly accurate as long as sufficient grid elements are available, and in very good agreement with the theoretical ray traveltimes. Note that in addition to our work presented in this paper, as far as we know the Coates and Schoenberg method has also been implemented by Nihei & Myer (2000) and Nihei *et al.* (2000) on

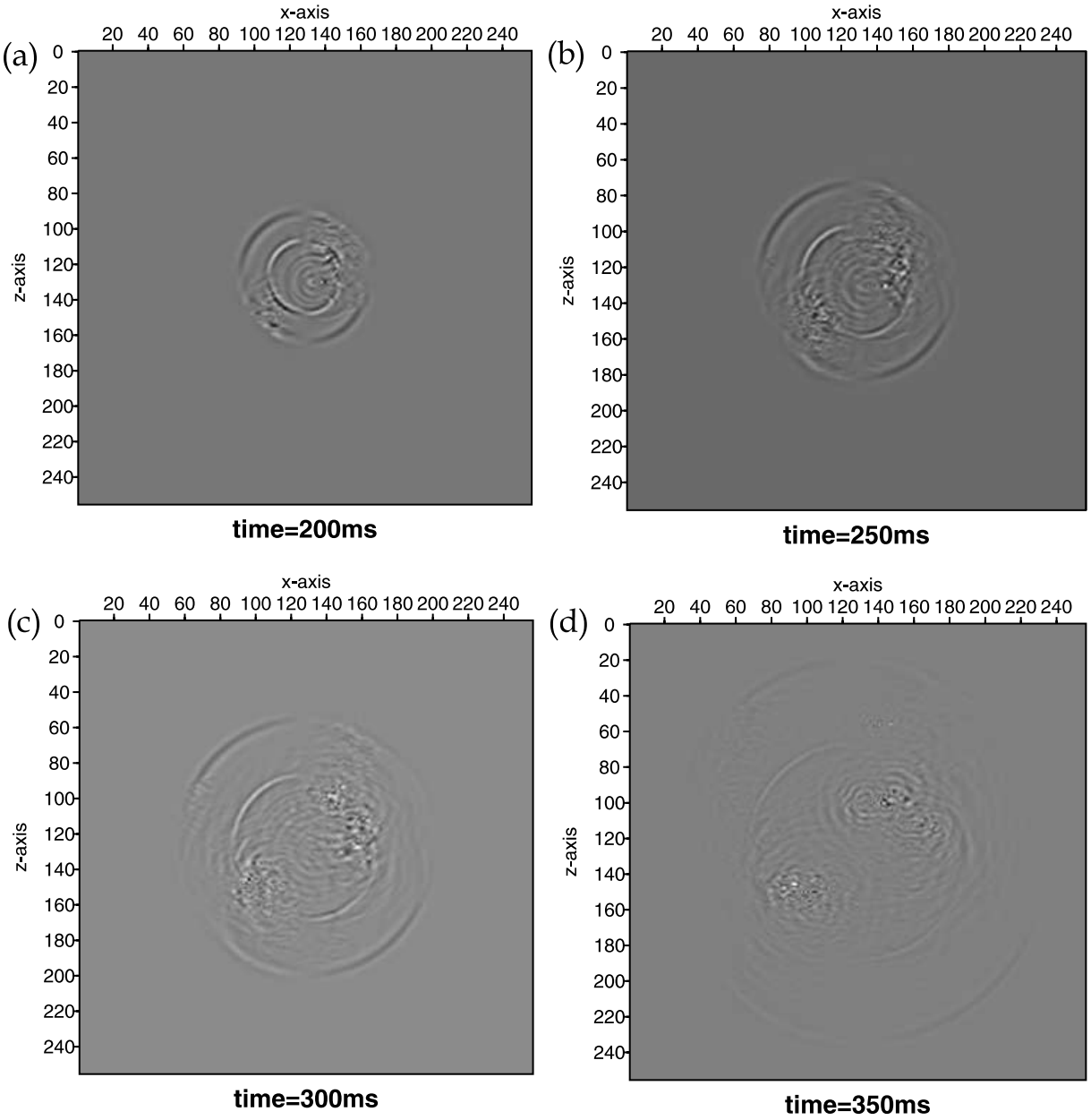

Figure 12. Snapshots from model in Fig. 11(a) taken at (a) $t = 200$ ms, (b) $t = 250$ ms, (c) $t = 300$ ms and (d) $t = 350$ ms.

staggered grid FDs, and by Chunlin Wu on variable grid FDs (Wu *et al.* 2002).

From the numerical examples we come to some interesting conclusions. First, we can see the importance of the spatial distribution of fractures in a medium. Our results show that in areas with fracture clustering, there is strong and coherent energy. Also, high clustering does result in high local fracture densities, which can cause the energy to be trapped in a certain area (localization processing), increasing the complexity of the wavefield and making individual phases and their identification very complicated. Also, we observe that different spatial distributions give different frequency content on the recorded wavefield. This as we might expect means that frequency-dependent seismic scattering depends on the spatial distribution of fractures (Leary & Abercrombie 1994). In addition, also of great importance is the fracture size relative to the wavelength, independent of the spatial distribution. It is demonstrated that when fractures are smaller than the wavelength, they act as single scatterers and generate secondary wavefields, whereas when the size approaches the wavelength they act as individual interfaces and the wavefield is more complicated. To complete our study, we examined the case of fracture sizes that follow a power-law or fractal distribution. The wavefield generated shows very strong coda waves and is very complicated. The observation confirms the importance of spatial and scale length distributions in modelling fractured rock.

Numerical modelling techniques, such as those presented here, can be a useful tool in the understanding of the important role of fractures and their effects on wave propagation. The knowledge gained by such studies may ultimately lead to the extraction of valuable information concerning the fracture distributions in natural rocks, directly from seismic data. In addition, our method may potentially provide a test of fracture imaging using seismic methods (as demonstrated by Nihei *et al.* 2000), and characterization of fractured reservoirs based on the concept of seismic scattering.

6 COLOUR ONLINE

Colour versions of Figs 2, 3, 8 and B1 are available online at Blackwell Synergy, www.blackwell-synergy.com.

ACKNOWLEDGMENTS

We thank Kurt Nihei, Seiji Nakagawa and Michael Schoenberg (Lawrence Berkley National Laboratory), Chunling Wu (Stanford University), John Queen (Conoco Inc.), Zhang Zhongjie, Xinwu Zeng (Chinese Academy of Sciences), and our colleagues Patience Cowie, Mark Chapman and Simon Tod for useful discussion concerning natural fracture distributions and fracture modelling. We thank GJI reviewer Thomas Daley and an anonymous reviewer and Editor Michael Korn for their constructive comments. We also thank Joe Dellinger of BP for reminding us of the paper by Muir *et al.* (1992). This research is supported by the sponsors of the Edinburgh Anisotropy Project. This work is published with the permission of the Executive Director of the British Geological Survey (NERC) and the EAP sponsors: BP, Chevron, Conoco, DTI, ENI-Agip, ExxonMobil, Norsk Hydro, PGS, Phillips, Schlumberger, Texaco, Trade Partners UK and Veritas DGC.

REFERENCES

Alford, R.M., Kelly, K.R. & Boore, D.M., 1974. Accuracy of finite-difference modelling of the acoustic wave equation, *Geophysics,* **39,** 834–842.

Benites, R., Aki, K. & Yomogida, K., 1992. Multiple scattering of *SH* waves in 2-D media with many cavities, *Pure appl. Geophys.,* **138,** 353–390.

Bonnet, E., Bour, O., Odling, N.E., Davy, P., Main, I., Cowie, P. & Berkowitz, B., 2001. Scaling of fracture systems in geological media, *Rev. Geophys.,* **39,** 347–383.

Chapman, C.H. & Drummond, R., 1982. Body-wave seismograms in inhomogeneous media using Maslov asymptotic theory, *Bull. seism. Soc. Am.,* **72,** 277–317.

Coates, R.T. & Schoenberg, M., 1995. Finite-difference modeling of faults and fractures, *Geophysics,* **60,** 1514–1526.

Fornberg, B., 1988. The pseudospectral method: accurate representation of interfaces in elastic wave calculations, *Geophysics,* **53,** 625–637.

Hentschel, H.G.E. & Proccacia, I., 1983. The infinite number of generalised dimensions of fractals and strange attractors, *Physica D,* **8,** 435–444.

Hill, R., 1963. Elastic properties of reinforced solids: some theoretical principles, *J. mech. Phys. Solids,* **11,** 357–372.

Hsu, C.-J. & Schoenberg, M., 1993. Elastic waves through a simulated fractured medium, *Geophysics,* **58,** 964–977.

Hudson, J.A. & Knopoff, L., 1989. Predicting the overall properties of composite materials with small-scale inclusions or cracks, *Pure appl. Geophys.,* **131,** 551–576.

Kachanov, M., 1984. Elastic solids with many cracks and related problems, *Adv. Appl. Mech.,* **30**.

Leary, P.C. & Abercrombie, R., 1994. Frequency dependent crustal scattering & absorption at 5–160 Hz from coda decay observed at 2–5 km depth, *Geophys. Res. Lett.,* **21,** 971–974.

Liu, E. & Zhang, Z., 2001. Numerical study of elastic wave scattering by cracks or inclusions using the boundary integral equation method, *J. comp. Acoust.,* **9,** 1039–1054.

Liu, E., Crampin, S. & Hudson, J.A., 1997. Diffraction of seismic waves with application to hydraulic fracturing, *Geophysics,* **62,** 253–265.

Liu, E., Hudson, J.A. & Pointer, T., 2000. Equivalent medium representation of fractured rock, *J. geophys. Res.,* **105,** 2981–3000.

Lysmer, J. & Drake, L.A., 1972. A finite element method for seismology, *Methods Computat. Phys.,* **11,** Academic Press, New York.

Mal, A.K., 1970. Interaction of elastic waves with a Griffith crack, *Int. J. eng. Sci.,* **8,** 763–776.

Mikhailenko, B.G., 2000. Seismic modeling by the spectral-finite difference method, *Phys. Earth planet. Inter.,* **119,** 133–147.

Muir, F., Dellinger, D., Etgen, J. & Nichols, D., 1992. Modeling elastic wavefields across irregular boundaries, *Geophysics,* **57,** 1189–1193.

Nihei, K.T. & Myer, L.R., 2000. Natural fracture characterisation using passive seismic waves, *Gas Tips,* Gas Technology Institute, US Dept. of Energy and Hart Publications Inc.

Nihei, K.T., Nakagawa, S. & Myer, L.R., 2000. VSP fracture imaging with elastic reverse-time migration, *70th Ann. Int. Mtg.: Soc. of Expl. Geophys.,* 1784–1751.

Pointer, T., Liu, E. & Hudson, J.A., 1998. Numerical modelling of seismic waves scattered by hydrofractures: application of the indirect boundary element method, *Geophys. J. Int.* **135,** 289–303.

Press, W.H., Teukolsky, S.A., Vetterling, W.T. & Flannery, B.P., 1997. *Numerical Recipes in Fortran 77: the Art of Scientific Computing (Vol. 1 of Fortran Numerical Recipies),* pp. 266–283, Cambridge University Press, Cambridge.

Pyrak-Nolte, L.J., Myer, L.R. & Cook, N.G.W., 1990. Transmission of seismic waves accross single natural fractures, *J. geophys. Res.,* **95,** 8617–8638.

Ricker, N.H., 1977. *Transient Waves in Visco-elastic Media,* Elsevier, Amsterdam.

Saenger, E.H. & Shapiro, S.A., 2002. Effective velocities in fractured media: a numerical study using the rotated staggered finite-difference grid, *Geophys. Prosp.,* **50,** 183–194.

Sayers, C.M. & Kachanov, M., 1995. Microcrack-induced elastic wave anisotropy of brittle rocks, *J. geophys. Res.,* **100,** 4149–4156.

Schoenberg, M., 1980. Elastic wave behaviour across linear slip interfaces, *J. acoust. Soc. Am.,* **68,** 1516–1521.

Schoenberg, M. & Sayers, C.M., 1995. Seismic anisotropy of fractured rock, *Geophysics,* **60,** 204–211.

van Baren, G.B., Mulder, W.A. & Herman, G.C., 2001. Finite-difference modeling of scalar-wave propagation in cracked media, *Geophysics,* **66,** 267–276.

Wu, C., Harris, J.M. & Nihei, K.T., 2002. 2-D finite-difference seismic modelling of an open fluid-filled fracture comparison of thin-layer and linear-slip models, *72nd SEG Ann. Int. Mtg. Exp. Abs.: Soc. of Expl. Geophys.,* 1959–1962.

Wu, R.S., 1982. Attenuation of short period seismic waves due to scattering, *Geophys. Res. Lett.,* **9,** 9–12.

Wu, R.S. & Aki, K., 1985. Scattering characteristics of elastic waves by an elastic heterogeneity, *Geophysics,* **50,** 582–589.

APPENDIX A: EFFECTIVE COMPLIANCE OF A FRACTURED MEDIUM

Effective medium calculus is used to calculate the elastic parameters that are associated with a given cell through which a fracture passes. In the simple case of an unfractured cell, where the cell is occupied only by the background rock, the calculation of the compliance tensor is straightforward. Assuming that we know the elastic parameters of the host rock, we calculate the compliance tensor s^0_{ijkl} as follows:

$$\mu = \rho V_s^2, \tag{A1}$$

$$\lambda = \rho\left(V_P^2 - 2V_S^2\right), \tag{A2}$$

$$\left(s^0_{ijkl}\right)^{-1} = c_{ijkl} = \begin{bmatrix} \lambda+2\mu & \lambda & \lambda & 0 & 0 & 0 \\ \lambda & \lambda+2\mu & \lambda & 0 & 0 & 0 \\ \lambda & \lambda & \lambda+2\mu & 0 & 0 & 0 \\ 0 & 0 & 0 & \mu & 0 & 0 \\ 0 & 0 & 0 & 0 & \mu & 0 \\ 0 & 0 & 0 & 0 & 0 & \mu \end{bmatrix}, \tag{A3}$$

where V_P and V_S are the *P*- and *S*-wave velocities in the medium, respectively, c_{ijkl} is the 6×6 matrix form of the stiffness tensor for the unfractured medium, and λ and μ are the Lamé constants.

In the presence of fractures the average strain ϵ in an elastic homogeneous solid with volume V containing N_f fractures with surfaces S_r ($r = 1, 2, \ldots, N_\mathrm{f}$) can be written as

$$\epsilon_{ij} = \left(s^0_{ijkl} + s^f_{ijkl}\right)\sigma_{kl}, \tag{A4}$$

where $\boldsymbol{\sigma}$ is the average stress tensor, s^0_{ijkl} is the matrix compliance tensor in the absence of the fractures and s^f_{ijkl} is the extra compliance tensor resulting from the fractures. The additional strain is given by (Hill 1963; Hudson & Knopoff 1989),

$$s^f_{ijkl}\sigma_{kl} = \frac{1}{2V}\sum_{r=1}^{N_\mathrm{f}} \int_{S_r} \left([u_i]n_j + [u_j]n_i\right) dS, \tag{A5}$$

where u_i is the ith component of the displacement discontinuity on S_r and n_i is the ith component of the fracture normal. If all fractures are aligned with fixed normal n, we may replace each fracture in V by an average fracture having a surface area S and a smoothed linear slip boundary condition given by

$$[\bar{u}_i] = Z_{ip} t_p, \tag{A6}$$

where t_p is the traction on the fracture, $[\bar{u}_i]$ is the average displacement discontinuity on the fracture and the quantities $\{Z_{ip}\}$ depend on the interior conditions and infill of the fracture (Sayers & Kachanov 1995; Schoenberg & Sayers 1995). The traction t_p is linearly related to the imposed mean stress $\boldsymbol{\sigma}$ or, more precisely, to the traction $\sigma_{pq}n_q$ that would exist on the crack face if the displacements were constrained to be zero.

Liu *et al.* (2000) used a model of a simple fracture in an unbounded medium and proposed that the traction can be written as

$$t_p = \sigma_{pq} n_q, \tag{A7}$$

eq. (A6) becomes

$$[\bar{u}_i] = Z_{ip}\sigma_{pq} n_q. \tag{A8}$$

Inserting eq. (A8) into eq. (A5) and after some tensor algebra, we obtain

$$s^f_{ijkl}\sigma_{kl} = \frac{N_\mathrm{f} S}{4V}\left(Z_{ik}n_l n_j + Z_{jk}n_l n_i + Z_{il}n_k n_j + Z_{jl}n_k n_i\right)\sigma_{kl}, \tag{A9}$$

where S is the mean area of fracture; so the fracture induced excess compliance s^f_{ijkl} is

$$s^f_{ijkl} = \frac{D_\mathrm{f}}{4}\left(Z_{ik}n_l n_j + Z_{jk}n_l n_i + Z_{il}n_k n_j + Z_{jl}n_k n_i\right), \tag{A10}$$

where D_f is

$$D_\mathrm{f} = \frac{N_\mathrm{f} S}{V}. \tag{A11}$$

If the fracture set is statistically invariant under rotations about n, only two terms in $\boldsymbol{Z}$ are required (Schoenberg & Sayers 1995); a normal fracture compliance Z_N and a tangential compliance Z_T. Thus

$$Z_{ij} = Z_\mathrm{N} n_i n_j + Z_\mathrm{T}(\delta_{ij} - n_i n_j) = Z_\mathrm{T}\delta_{ij} + (Z_\mathrm{N} - Z_\mathrm{T}) n_i n_j, \tag{A12}$$

where δ_{ij} is the Kronecker delta. By inserting (A12) into (A10), we have

$$s^f_{ijkl} = \frac{D_\mathrm{f}}{4}[Z_\mathrm{T}(\delta_{ik}n_l n_j + \delta_{jk}n_l n_i + \delta_{il}n_k n_j + \delta_{jl}n_k n_i) + 4(Z_\mathrm{N} - Z_\mathrm{T}) n_i n_j n_k n_l]. \tag{A13}$$

Following Coates & Schoenberg (1995), in the case of 2-D media in a grid cell intersected by a fracture, eq. (A11) becomes

$$D_\mathrm{f} = \frac{N_\mathrm{f}\Delta l}{\Delta A}, \tag{A14}$$

where Δl is the length of the segment of the fracture lying within the cell and ΔA is the area of the 2-D cell. If L is defined for each cell intersected by a fracture so that

$$\frac{1}{L} \equiv \frac{\Delta l}{\Delta A}, \tag{A15}$$

then eq. (A13) finally becomes

$$s^f_{ijkl} = \frac{N_\mathrm{f}}{4L}[Z_\mathrm{T}(\delta_{ik}n_l n_j + \delta_{jk}n_l n_i + \delta_{il}n_k n_j + \delta_{jl}n_k n_i) + 4(Z_\mathrm{N} - Z_\mathrm{T}) n_i n_j n_k n_l], \tag{A16}$$

which is the equation we use for the calculation of the excess compliance tensor. So the induced excess compliance tensor of a cell depends on the normal Z_N and the tangential Z_T fracture compliance, the number N_f of the fractures inside the cell, the length Δl of each fracture (or segment of fracture) and the orientation of each fracture estimated by the normals n. The total compliance tensor for the fractured cells is the effective compliance tensor s^{eff}_{ijkl}, which characterizes the cell and is

$$s^{\mathrm{eff}}_{ij} = s^0_{ijkl} + s^f_{ijkl}. \tag{A17}$$

If we want to determine the stiffness c_{ijkl}, we transform s_{ijkl} to the conventional (two-subscript) condensed 6×6 matrix notation, $11 \rightarrow 1, 22 \rightarrow 2, 33 \rightarrow 3, 23 \rightarrow 4, 13 \rightarrow 5, 12 \rightarrow 6$, with factors of 2 and 4 introduced as follows: $s_{ijkl} \rightarrow s_{pq}$ when both of P, q are 1, 2, or 3; $2s_{ijkl} \rightarrow s_{pq}$ when one of p, q is 4, 5 or 6; and $4s_{ijkl} \rightarrow s_{pq}$ when p, q are any of 1, 2, 3, 4, 5 or 6. The inverse of the compliance matrix s_{pq} gives the effective elastic constants or stiffness matrix c_{pq}. Using the same transformation as for the compliance, we transform the stiffness from the condensed (two-subscript) to the normal notation ($c_{pq} \rightarrow c_{ijkl}$).

APPENDIX B: EFFECTS OF FRACTURE TIPS

An important parameter in the accurate modelling of natural fractured rocks is the realistic implementation of the effects of fractures in wave propagation. The main issue is the realistic representation of the finite extent of a fracture, and especially the two fracture tips. To exhibit the end of the fracture at both tips, we should have no displacement outside those points, thus the compliance tensor $\boldsymbol{Z}$ should be 0. A way of expressing the change in the compliance is to keep the compliance constant along the fracture and drop to 0 at the crack tips. However, the sudden drop of the value is not very realistic, and there is no similar case in natural systems that demonstrates extreme changes of values. We believe that it is more realistic to represent the changes in $\boldsymbol{Z}$ as a gradual reduction towards 0 at the fracture tips. Following Kachanov (1984) the compliance at each point of the fracture is given by

$$\boldsymbol{Z} = Z_{\max}[1 - (x/l)^2]^{1/2}, \tag{B1}$$

where $Z_{\max}$ is the maximum value of the compliance in the centre of the fracture, l is half the length of the fracture and x is the x-coordinate of the position of a point in the fracture. The coordinates of the right and the left fracture tips are $+l$ and $-l$, respectively. From eq. (B1), for the centre of the fracture ($x = 0$) the compliance is $\boldsymbol{Z} = Z_{\max}$, whilst for the fracture tips ($x = \pm l$) the compliance is $\boldsymbol{Z} = 0$. So the value of the compliance is maximum in the centre of the fracture and reduces gradually following a hyperbolic function until it reaches 0 in both fracture tips. As we can see from eq. (B1) the rate of reduction depends on the size $2l$ of the fracture, so the larger the fracture, the more gradually the compliance reduces.

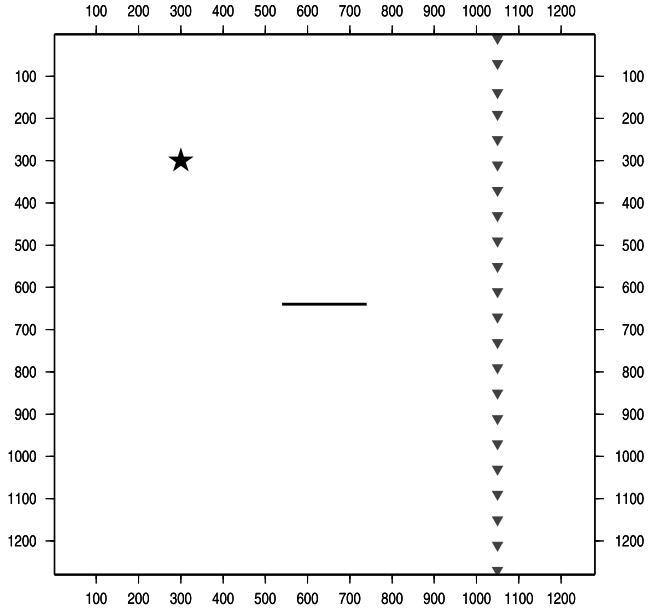

Figure B2. Model used to examine the effect of the fracture tips on the wavefield.

In Appendix A we described the implementation of fractures in the finite-difference grid and the calculation of the effective compliance of a fractured medium. Eq. (A16) calculates the excess compliance tensor, which expresses the fracture influence. The excess compliance tensor is estimated for each of the fractured grid cells of the medium, thus the value of the compliance $\boldsymbol{Z}$ should remain constant inside each grid cell. To calculate the compliance for each of the grid cells, from eq. (B1) we find the values of the compliance for the two nodes of each cell, and take the average of the two values as the effective value of the compliance throughout the cell. This is illustrated in Fig. B1, where the curve represents the value of the compliance following eq. (B1), and the stepped line is the average

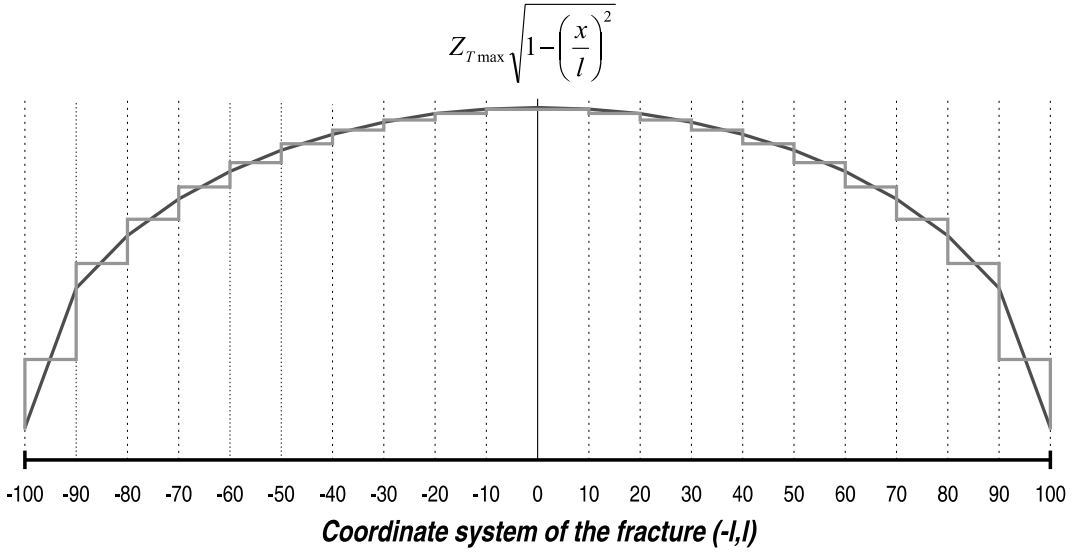

Figure B1. Schematic representation of the reduction of the value of compliance $\boldsymbol{Z}$ along a fracture. The curve represents the value of compliance following eq. (B1) of Kachanov (1984). The stepped line represents the way we approximate that function in our implementation.

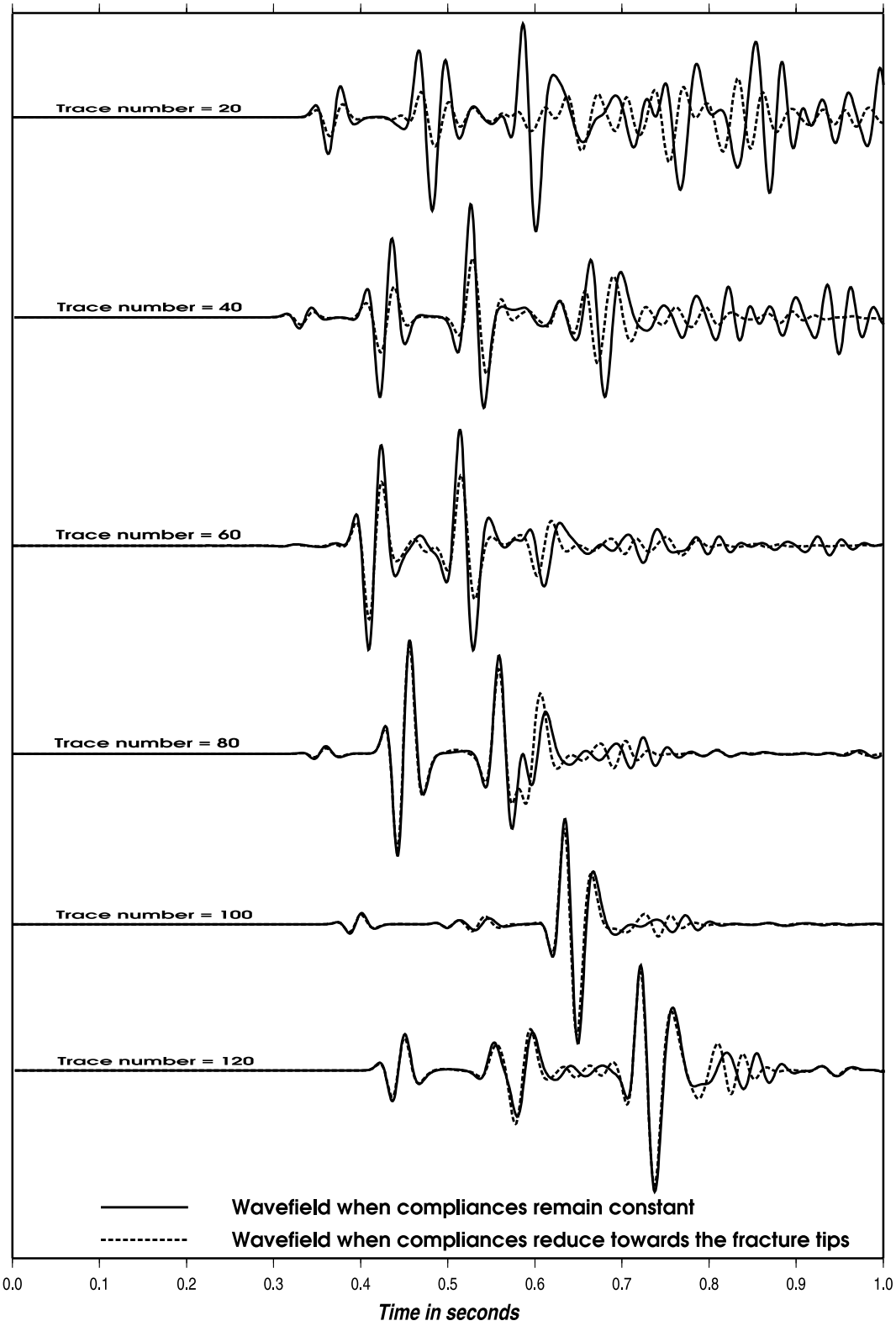

Figure B3. Comparison of the wavefields generated by two different implementations of the fracture compliance. Solid-line wavelets represent the case of a constant compliance that drops to 0 at the fracture tips, while dotted-line wavelets represent our implementation, based on Kachanov's (1984) concept, where the compliance reduces gradually. The trace numbers correspond to depths 200, 400, 600, 800, 1000 and 1200 m.

value of the compliance we use for each grid cell. In the case where a grid cell is intersected by multiple fractures (or parts of fractures) the compliance is taken to be the average value of the compliances arising from each of the fractures independently.

To understand the effect of the fracture tips on the wavefield, we model the case of a single fracture in which, in the first case, the compliance remains constant throughout the fracture and drops to 0 at the tips, and, in the second case, the compliance reduces

following our implementation. The model we use is presented in Fig. B2. For the two cases we compare the wavelets of a number of traces and the results are presented in Fig. B3. The wavelets presented in Fig. B3 do not include direct waves, because they are not affected by the fracture tips, and so are identical. Also, the amplitude of the wavelets is normalized between the several traces. However, the relative amplitude between the wavelets for each individual trace remains accurate. From the comparison between the wavelets, we first observe that there is a time difference between the *SS* waves when we have constant compliance and when the compliances reduce gradually, with *SS* waves of the latter case being slower. This may be a result of the sensitivity of *S* waves to changes of anisotropy. By changing the compliance from constant to variable, we effectively change the anisotropy, and this is only visible in the *SS* wavelets. However, when we observe the wavelets from traces 100 and 120 we see that the time difference in the *SS* waves disappears. The waves observed at those receivers come from waves diffracted from the crack tips and from waves refracted at the fracture, in contrast to the rest of the receivers, where we have diffracted and reflected waves. Also, we can observe variations in the amplitude. In traces 20, 40 and 60, where the receivers are above the fracture, so we have reflected and diffracted waves, the amplitude of the waves when the compliance is constant is higher than the amplitude when the compliance follows our implementation. On the other hand, in trace 80, when the waves are only diffracted, we have opposite results. Finally, in traces 100 and 120, where we have refracted and diffracted waves, the amplitudes seem to be almost identical. We see that reflection and refraction are decisive factors in the wavelet pattern. More research needs to be done on these topics to examine how they affect the waves.

Another parameter that we have not examined is the effect of the length of the fracture. From eq. (B1) we can see that if we have a fracture of short length l then the reduction of the compliance would be severe, whilst when the fracture is very large we will have a very smooth reduction that can approximate the case of the constant compliance throughout the fracture. This has to be tested by modelling various sizes of fractures and the respective wavelets, to find out at what point the approximation of constant compliance is satisfactory.

APPENDIX C: GENERATION OF FRACTURE DISTRIBUTIONS

Scaling in fracture systems has become an active field of research over the previous 25 years motivated by practical applications. In the case of the hydrocarbon industry, scaling laws provide a key to predicting the nature of subseismic fracturing (below the limit of seismic resolution), which can significantly influence reservoir and cap rock quality, from seismically resolved faults. The numerous studies of fracture-system scaling in the literature do indeed suggest that scaling laws exist in nature. They also indicate, however, that such scaling laws must be used with caution and with due regard to the physical influences that govern their validity. Over recent years the power-law distribution has been increasingly employed to describe the frequency distribution of fracture properties and geometry. However, a power law is not an appropriate model in all cases, and other distributions that have been used include the log-normal, gamma and exponential laws.

In the main part of this paper, we examine the effect of different spatial distributions of fractures on the wave propagation. The fractures are distributed as follows: (a) a random uniform, (b) a Gaussian, (c) an exponential and (d) a Gamma distribution, as shown in Fig. 4. The algorithm utilizes a different random number generator (Press *et al.* 1997), which varies according to the distribution we want to simulate. For each distribution, the generator is applied once to give x-coordinates, and completely independently once more to give z-coordinates. Both x- and z-coordinates are afterwards normalized to the grid size of the model.

These pairs of x- and z-coordinates are the centres of the distributed fractures. The resulting distribution of fractures, without any alterations, is the parent spatial distribution. The size and orientation of the fractures are given as an input to the algorithm. In this paper all the fractures are parallel to the grid. Subsequently, the algorithm examines the fractures for any overlapping cases. We define overlapping as the case where the distance between the centres of two fractures is less than a predefined value. In the current application of the algorithm, we examined only the horizontal distances between pairs of fracture centres having the same z-coordinate. For simplicity in this paper we deliberately avoid modelling intersected cracks, that is, conjugate fracture sets. However, in theory, such a case can also be modelled with the method we use. In this case, the second overlapping fracture is excluded from the distribution. After testing for overlapping, the remaining number of distributed fractures is counted. If that number is less than desired, the resulting distribution of fractures is rejected. The number of fractures following the parent spatial distribution is raised by 5. A new group of fractures, spatially distributed according to the parent distribution, is chosen. The new group of fractures follows the same procedure that we described above. This process continues until the desired number of non-overlapping spatially distributed fractures is reached. A flow chart of the filtering algorithm is presented in Fig. C1. The final spatial distribution of the fractures is a result of the parent distribution after applying data filtering, so we call this the daughter spatial distribution. The spatial correlation in the daughter population is then determined by the two-point correlation function of the fracture centre locations in two dimensions. Figs C2–5 show the independent probabilities $P(x)$ and $P(z)$ as a function of the x- and z-coordinates of the centres of the fractures, for the daughter distributions (a)–(d) of Fig. 4. In the same figures we show the two-point correlation function $C(r)$, for each of the four parent distributions, defined as

$$C(r) = \frac{1}{N^2} N_d(r), \tag{C1}$$

where N is the total number of points and N_d is the number of pairs of points where the distance is less than r (Hentschel & Proccacia 1983).

The probability plots in Figs C2–5 confirm that the random number generator does create random uniform, Gaussian, exponential and Gamma distributions, respectively, of centres of fractures along the two grid directions. The two-point correlation functions of the parent spatial distributions, are shown in Figs C2(c), C3(c), C4(c) and C5(c). The random uniform distribution has correlations that peak in the medium range, the Gaussian and the exponential peak in the short range, and the Gamma is the most broad-band distribution. Thus the ratio of wavelength to correlation length will be greatest for the random uniform distribution, and smallest for the Gamma distribution.

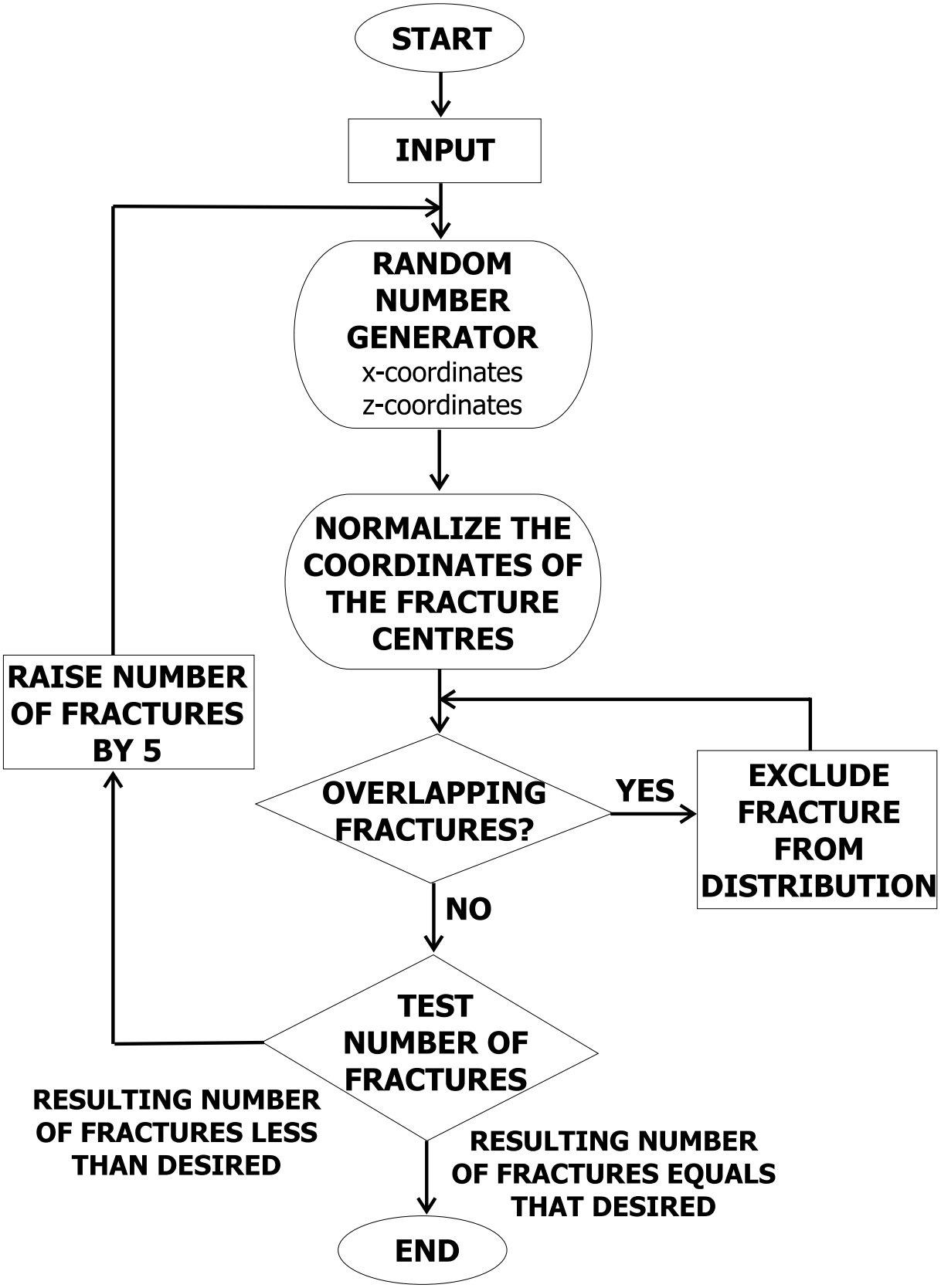

Figure C1. Flow chart of the algorithm used to generate the four spatial distributions of fractures shown in Fig. 4.

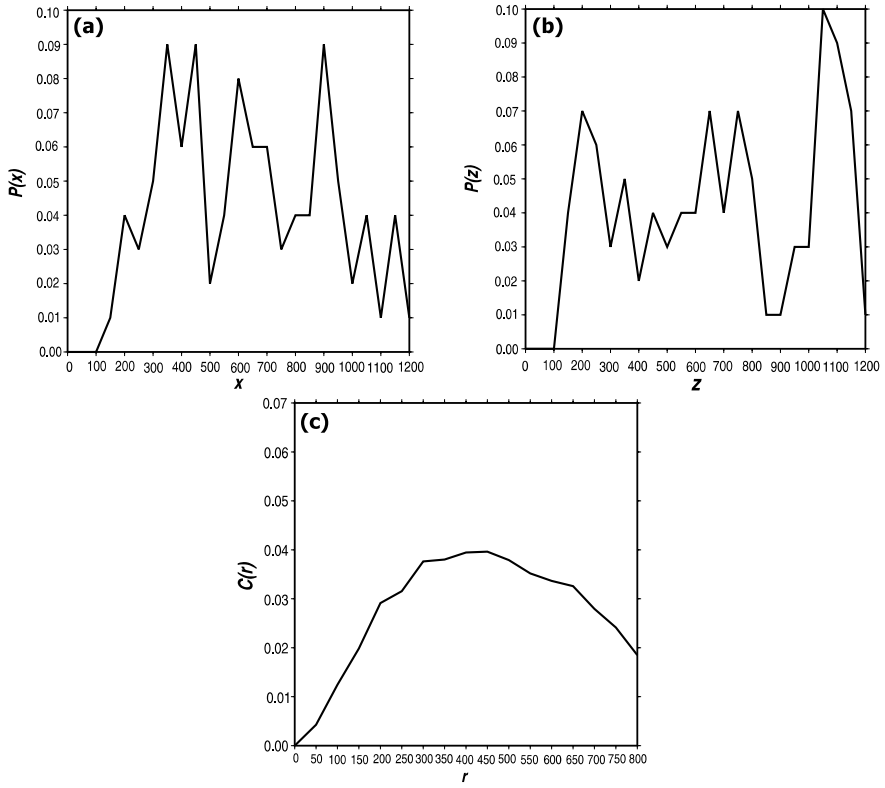

Figure C2. Statistical properties of the random uniform distribution of fractures in Fig. 4(a). (a) Probability plot of the coordinate of the centre of fractures along the *x*-direction, (b) probability plot of the coordinate of the centre of fractures along the *z*-direction, (c) two-point correlation function of the parent distribution of fractures.

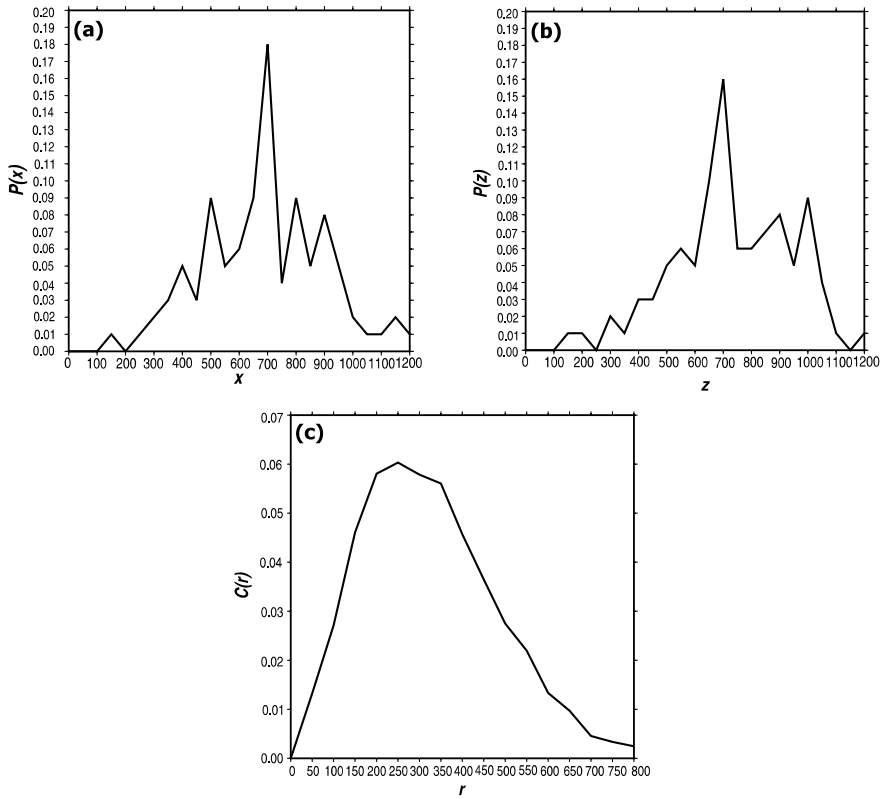

Figure C3. Statistical properties of the Gaussian distribution of fractures in Fig. 4(b). (a) Probability plot of the coordinate of the centre of fractures along the *x*-direction, (b) probability plot of the coordinate of the centre of fractures along the *z*-direction, (c) two-point correlation function of the parent distribution of fractures.

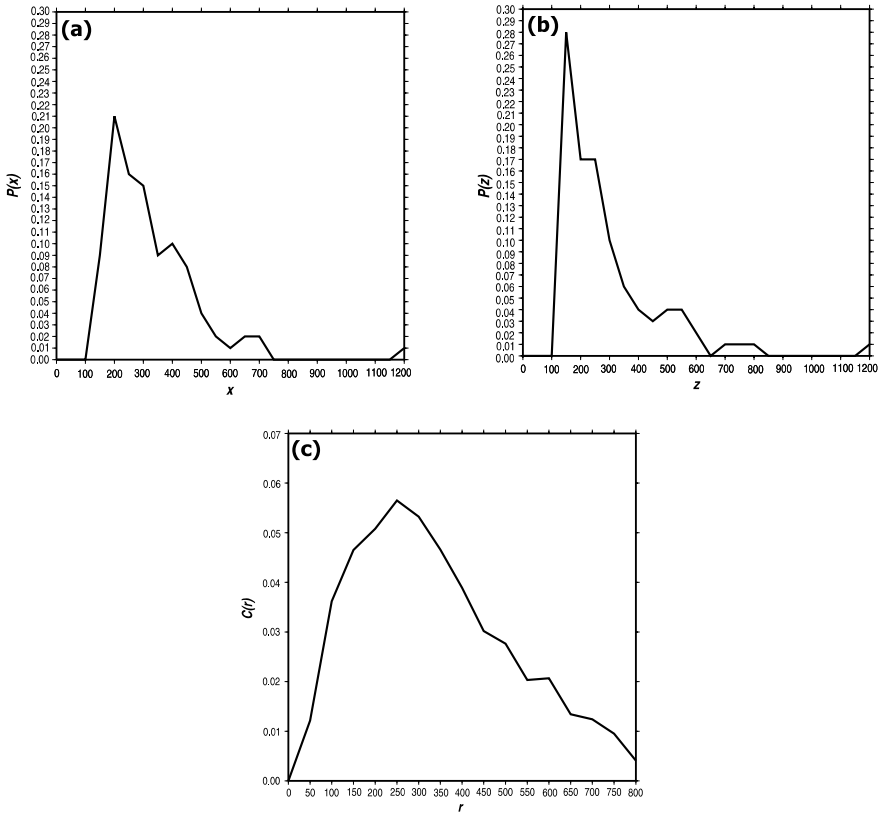

Figure C4. Statistical properties of the exponential distribution of fractures in Fig. 4(c). (a) Probability plot of the coordinate of the centre of fractures along the *x*-direction, (b) probability plot of the coordinate of the centre of fractures along the *z*-direction, (c) two-point correlation function of the parent distribution of fractures.

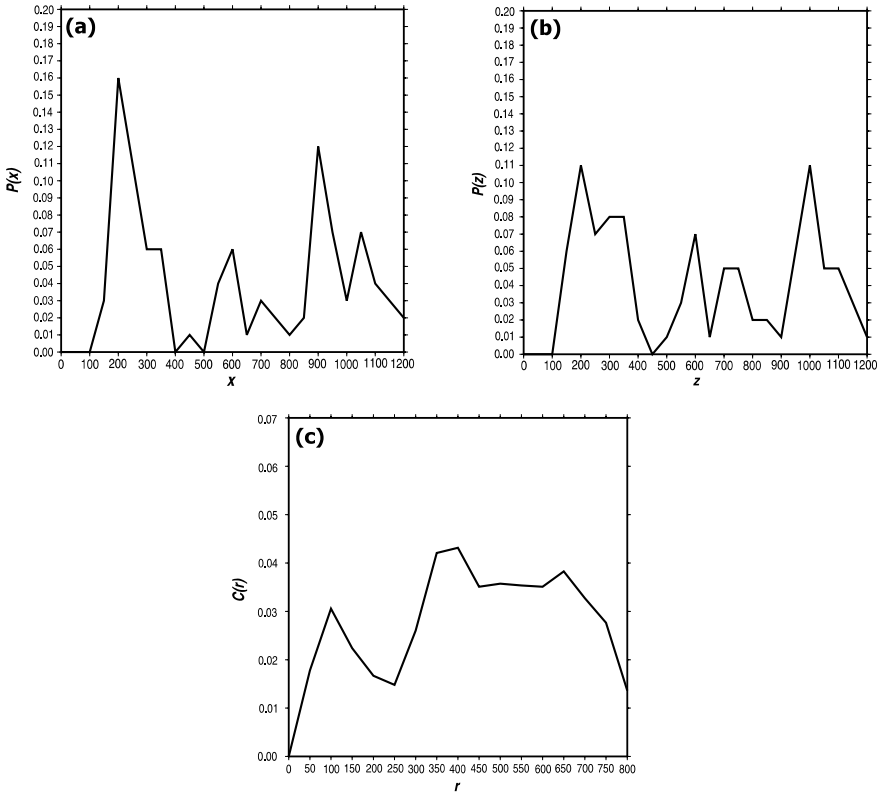

Figure C5. Statistical properties of the Gamma distribution of fractures in Fig. 4(d). (a) Probability plot of the coordinate of the centre of fractures along the *x*-direction, (b) probability plot of the coordinate of the centre of fractures along the *z*-direction, (c) two-point correlation function of the parent distribution of fractures.